MET O 11 Technical Note No 157

A Study of the Structure of Mid-Latitude Depressions in a Numerical Model using Trajectory Techniques. I. Development of a Baroclinic Wave in a Dry Atmosphere.

by

B. Golding

Meteorological Office
Forecasting Research Branch
London Road
Bracknell
Berkshire
United Kingdom

May 1982.

VS

A Study of the Structure of Mid-Latitude Depressions in a Numerical Model using Trajectory Techniques. I Development of a Baroclinic Wave in a Dry Atmosphere.

by

B Golding

ABSTRACT

Trajectory tracing techniques are used to investigate the structure and airflow of a developing baroclinic wave simulated by a numerical atmospheric forecast model. Three stages are described. The structure of the linear stage is explained with reference to the normal mode theory of baroclinic instability. In the mature stage, flow separation zones form which are identified as warm and cold fronts. At the occluded stage, circulation of cold air round the centre of the depression leads to changes in the structure of the cold front. Comparisons are made with previously published integrations by specially constructed models in order to establish a basis for comparison of forecasts from real data which will appear in future papers.

A Study of the Structure of Mid-Latitude Depressions in a Numerical Model using Trajectory Techniques. I Development of a Baroclinic Wave in a Dry Atmosphere.

1. INTRODUCTION

The work described in this paper forms part of an attempt to relate the observed features of mid-latitude depressions to the theory of baroclinic wave development. Future papers will describe investigations in which the techniques developed here are applied to baroclinic wave development in a moist atmosphere, and to integrations from real initial states.

The theory of baroclinic waves was established in the papers of Eady (1949) and Charney (1947) using a perturbation analysis of the quasi-geostrophic equations. The instability in the solutions was interpreted as a wave which drew energy from the mean thermal gradient of the initial state. The resultant eddies were tentatively identified with the familiar depressions of the mid-latitude westerlies despite exhibiting none of the synoptic scale weather features associated with such systems. The theory has advanced in many ways since then. Basic states other than a uniform jet on an f plane have been investigated (Green 1960, McIntyre 1970, Simmons & Hoskins 1976). Work has also been done on the non-linear development of the waves using both analytical (Pedlosky 1970) and numerical techniques (Mudrick 1974). It can be shown that the quasi-geostrophic approximation becomes locally invalid in the non-linear stage and the understanding of developments at this stage has been greatly increased by the use of

the semi-geostrophic equations (Hoskins and Bretherton 1972, Hoskins 1975, Hoskins and West 1979).

Observational studies of mid-latitude depressions have a longer history and started as soon as the exchange of simultaneous weather observations was first made possible by the invention of the telegraph. The basic synoptic scale description was established by the Bergen school (Bjerknes 1918, Bjerknes and Solberg 1922) and was altered in detail only by the advent of regular upper air soundings. More recent studies have concentrated on the meso-scale structure of parts of depressions rather than the overall structure of the whole system.

The object of the present work is to try to fill in some of the ground separating these two branches of study. The vehicle chosen for the attempt is a numerical model designed for routine weather forecasting. There are inherent weaknesses in the approach. The grid-length in such a model is too large to represent most of the features observed in detailed studies of real depressions. However, it is well established that such models can make a creditable attempt at reproducing the observed synoptic scale features even when their true scale is of the same order as the model grid-length. From the theoretical viewpoint, a forecast model includes a variety of smoothing processes which keep it stable in real forecasts but which may obscure the details of baroclinic wave development. Also, by using the full primitive equations, a large number of different processes will be represented by the model which may not be much easier to separate in the model solutions than they are in the atmosphere. These criticisms can be tackled by relating the model

results to theoretical studies using specially constructed models. By doing this, the ability of the forecast model to reproduce the theoretical results can be established. At the same time a link can be made between the forecast model behaviour and the hierarchy of research relating the latest theoretical models to simpler models and ultimately to the linear instability problem. Once this link has been made, the forecast model results for real situations may be related to its behaviour in the idealised situation. This is difficult to do using conventional displays of temperature, wind velocity etc. In the present work, the main tool for analysing these structures is the calculation of air parcel trajectories. Trajectory computation has been used as an analytical technique in meteorology for some time. Djuric (1961) demonstrated the application of computers to the problem and concluded that gaps in the observational network were the main hindrance to accurate computation. Danielson (1961) also investigated the accuracy of trajectory calculations and demonstrated the benefits of isentropic analysis as a way of computing vertical motions. These techniques were extended by Green, Ludlam & McIlveen (1966) who described the circulation in mid-latitude depressions by a simple consideration of isentropic trajectories. Difficulties remained with the technique, however, due to the poor space and time resolution of the observing network. In field experiments such as that reported in Browning & Harrold (1969) considerable use is made of the assumption of stationarity in the system structure in order to use frequent observations at a single location to obtain a detailed isentropic analysis from which to compute trajectories. Unfortunately such assumptions are rarely justified except as a first approximation. Numerical models have considerable advantages over observations in

this respect. Not only are the data available on a regular grid at frequent intervals, but they are self consistent and do not suffer from aliassing problems since small scale features cannot be represented in the model. An example of trajectory computations for a depression in a general circulation model was given in Gilchrist (1971). The consistent specification of vertical velocity in numerical models removes the need to use isentropic coordinates to obtain trajectories and has the advantage of adequately dealing with large scale diabatic sources. The remaining source of error, apart from that in the forecast itself, lies in the sub grid-scale mixing processes, primarily convection. In this paper it will be demonstrated that trajectories provide a particularly useful means for analysing the non-linear development of a baroclinic wave, particularly in the frontal regions. Together with a comparison of diagnostic fields with those obtained by Hoskins & West (1979), this will provide the necessary basis for comparison required for studies of real systems.

2. TECHNIQUES.

The numerical forecast model used for the studies was the U.K. Meteorological Office Operational Model (Burridge and Gadd 1977, Gadd 1978a, 1978b, 1980). It is a pressure coordinate model with 10 equally spaced levels at 100mb intervals. The horizontal grid is defined on a polar stereographic projection of the earth's surface. For the baroclinic wave integration, the coarse mesh, Octagon version was used which has a grid length of 300 Kms at 60°N and covers most of the Northern Hemisphere north of 20°N. The grid is staggered with horizontal velocity components at the centre of each grid square and

vertical velocity at mid-level. The split explicit time integration scheme (Gadd 1978a) is used with a time step of 30 mins. Orography was set to zero everywhere and all physical processes were removed except horizontal diffusion and a convective adjustment procedure which are needed to preserve stability. The model was integrated for 7 days and values of height and velocity were output at every grid point and level each hour. The velocity components were interpolated to trajectory locations directly from their staggered positions to avoid unnecessary smoothing. The interpolation was linear in the three coordinate directions. Integration of the trajectory equation was performed using the following algorithm

$$\underset{\sim}{x}^{n+\frac{1}{2}} = \underset{\sim}{x}^{n} + \underset{\sim}{u}^{n}(\underset{\sim}{x}^{n}) \cdot \frac{\Delta t}{2}$$

$$\underset{\sim}{x}^{n+1} = \underset{\sim}{x}^{n} + \underset{\sim}{u}^{n+\frac{1}{2}}(\underset{\sim}{x}^{n+\frac{1}{2}}) \cdot \Delta t \qquad (1)$$

where $\underset{\sim}{x}$ is position, $\underset{\sim}{u}(\underset{\sim}{x})$ is the interpolated model velocity at position $\underset{\sim}{x}$ and n is the time level. Since $\underset{\sim}{u}$ is available from the model every hour, this yields a new value of $\underset{\sim}{x}$ every two hours. Diagnostic quantities such as vorticity and temperature were produced in map form for a part of the forecast domain and were also interpolated to trajectory positions. Details of the calculation of these quantities are given in Golding (1981). Checks were performed to verify that the trajectories gave a true representation of the air flow in the model. No significant difference was found when the data were obtained from the model every 30 mins and trajectory positions computed every hour. Results obtained using the model velocities as in Eq 1 were compared with others obtained from the model height field using the Lagrangian form of the momentum equations to predict $\underset{\sim}{u}$ -

$$\frac{d\underset{\sim}{u}}{dt} = -f\hat{\underset{\sim}{k}} \wedge \underset{\sim}{u} - g\nabla h + \text{map projection terms} \qquad (2)$$

Again the results were very similar, but rather rougher especially in frontal regions. No significant difference in mean path could be seen and since the roughness made the results more difficult to interpret, the use of Eq 1 was preferred. Conservation of potential temperature by individual parcels was satisfied within the error of interpolation from mean layer temperatures, except by a few parcels in frontal regions at the occluding stage. By contrast, the vorticity equation

$$\frac{d(\zeta+f)}{dt} = -\mathcal{D}(\zeta+f) - \left(\frac{\partial v}{\partial p}\frac{\partial \omega}{\partial x} - \frac{\partial u}{\partial p}\frac{\partial \omega}{\partial y}\right) \qquad (3)$$

where ζ is relative vorticity and $\mathcal{D}$ is divergence, was very poorly satisfied. The error could not be explained by diffusion or minor map projection corrections. Ultimately, it was found that the model integration scheme performs a considerable smoothing on the divergence term. Details of the analysis are given in the Appendix but rough calculation shows that the size of this term could be reduced by half in frontal regions. This explains the discrepancy in the trajectory results and is also the most likely reason for the low vorticities found at the mature and occluding stages compared with those obtained by Hoskins and West (1979).

In order to look at the stages of development of the wave, trajectories were computed for 48 hour periods starting at several times in the forecast. In each case an initially square grid of parcels was started at two levels (750mb and 950mb) and the subsequent motion displayed relative to the motion of the surface low pressure centre. The trajectories are displayed by plotting the positions as a series of crosses whose size varies linearly with pressure and is zero 100mb below the starting level. (No parcels

descend by more than 100mb in 48 hours). At the later stages of development a selection of the tracks is plotted to reduce the confusion of many crossing lines. These diagrams are interpreted schematically in terms of regions of flow with some of the boundaries identified as fronts. Figure 1 shows a pair of such diagrams for the mature stage. Here, an arrow which thickens towards its head indicates ascent. Region A denotes the flow of cold air round the north side of the system. Regions B and C are warm air which rises at the warm front. Region B denotes such air when it turns to the left relative to the system, and region C is that which turns to the right. Region D is the flow under the warm front towards the centre which generally shows some ascent.

3. DEVELOPMENT OF A BAROCLINIC WAVE

a) Initial Conditions

A broad jet was specified as the unperturbed state and a small wavenumber 6 perturbation superimposed on it. Figure 2 shows the vertical and meridional structure of the jet. It has a maximum speed of nearly $39 ms^{-1}$ at $45^{\circ}N$ and 200mb. The geopotential field was obtained from the perturbed motion field by solution of a reverse balance equation. At 1000mb the perturbation amplitude in the geopotential field was 17m. The pole to equator temperature contrast at 550mb was a little over 25K.

b) Linear stage

The early stages of development will be summarised by looking at the 72 hour diagnostics and trajectories for the period 48-96 hours. Figure 3a shows the 1000mb height field. The range of values is 74m corresponding to about 10mb pressure difference at the surface. At

500mb (Fig 3b) a pronounced trough has formed with its axis near 25°W, some 15° west of the surface centre. The amplitude of the disturbance is 60 metres at 50°N near the centre of the jet. The 1000mb relative vorticity field is shown in Fig 3c. An arrowhead shaped pattern is evident with a maximum of $10^{-5}s^{-1}$ near the surface pressure centre and arms of positive vorticity extending northwest and southwest from it. The 550mb vertical velocity pattern (Fig 3d) shows very small values (less than $0.5\mu bs^{-1}$) everywhere. Ascent is greatest near 50°N 5°W, about 5° east of the surface centre, with regions of ascent extending to the northwest and south-southwest from there.

A set of trajectories was initiated at 48 hours on a grid covering the region around the low pressure centre. Figure 4 shows the tracks of parcels initially at 950mb. The almost constant size of the crosses indicates that little vertical motion is occurring. The parcels near the top left of the diagram show little evidence of a disturbance. Nearer the bottom of the diagram, parcels entering from the right deviate northwards with slight ascent while parcels being left behind by the disturbance go southwards and descend a little. At 750mb (Fig 5) an almost circular pattern is found since the system speed is close to the mean wind speed at this level. Here, there is clear indication of ascent ahead of the centre and descent behind it. However, there is no evidence of the flow dividing into distinct regions as will be found at later stages.

c) Mature stage

The mature stage of development is the time when the central pressure deepens most rapidly and the main non-linear features of the flow appear. The period around 120 hours best represents this stage. Figure 6a shows the 1000mb height field at that time. The low centre has moved northeastwards giving a pronounced asymmetry between the high and low pressure areas. The height range is now 238m (about 32mb in surface pressure) and the deepening of the low in the previous 24 hours was 66m. A pronounced trough south from the low centre can be traced to cross 0° longitude at about 43°N. There is also a slight indication of a trough at 49°N 18°E extending southeast from the centre. The 500mb height field is shown in Fig 6b. The trough axis is at about 5°W, 10° west of the surface centre, and shows some asymmetry due to the effects of the non-linear advection terms in the equations of motion. The 1000mb relative vorticity field (Fig 6c) has its maximum of cyclonic vorticity at 53°N 9°E, just east of the surface pressure centre, and has an east-west orientation. From its eastern end, a secondary maximum extends southwestwards, parallel to the pressure trough and slightly ahead of it. The eastern end of the vorticity maximum is also the location of maximum ascent at 550mb (Fig 6d). The orientation of these features can be related to the low level temperature structure shown in Fig 6e. Both pressure troughs lie on the 275K isotherm. Note, however, that the tightest part of the thermal gradient, in the region east of the centre, is ahead of this between the 265K and 270K isotherms. In order to clarify the relationship between the diagrams presented above, Fig 6f is a composite of their main features. The region of maximum vorticity (solid line) is almost entirely enclosed by the region of

ascent (dashed line). The region of tight thermal gradient to the southwest of the centre lies partly in a region of descent and is behind the line of the secondary vorticity maximum. By contrast, the region of tight thermal gradient to the east of the centre lies within the regions of high vorticity and ascent, and the maximum of both quantities lies close to the 275K isotherm. The maximum ascent (L_ω) occurs at the eastern extremity of the region of high vorticity which is also the eastern end of the region of tightest thermal gradient.

These results may be compared with day 5 of the integration described in § 4e of Hoskins and West (1979). Although their integration was performed using a channel model with cyclic boundary conditions, the structure of the basic jet and the scale of the perturbation are similar to those used here. In particular, the doubling time of their perturbation (1.3 days) is very close to that observed in the present results. Their Fig 8 showed height and temperature fields at the lower boundary of the model at 5 days. It can be compared with the 1000mb height fields and 950mb temperature fields presented above but exact agreement is not expected since the present model applies its lower boundary condition at the ground, not at 1000mb. The range of height is 250m in Hoskins & West compared with 238m in fig 6a. The shape of the temperature wave is also very similar. However, the maximum vorticity at this stage of their integration was nearly double the value of $6 \times 10^{-5} s^{-1}$ shown in Fig 6c (personal communication). This can be related to two differences between the models. Firstly, the use of the geostropic coordinate transformation permits effectively higher resolution in regions of high vorticity while the diffusion term in the present model will result in some vorticity diffusion.

A grid of air parcel trajectories was initiated at 96 hours over a region covering the low pressure centre and followed for 48 hours. Fig 7 shows a selection of tracks of parcels initially at 950mb. The flow can now be divided into distinct regions. Between them are two separation zones across which parcels do not usually flow and which divide air coming from quite different origins. On this basis they are identified as fronts and marked with the usual symbols on the schematic. The separation zone marked by the cold front symbol divided regions A and B. That is, it separates cold air which has passed the northern side of the system and is travelling southwest away from the centre, from warm air which has been drawn into the southern side of the system and is being accelerated to the northeast by the strengthening pressure gradient near the centre. On the trajectory diagram (Fig 7a) it shows up as a narrow region with air travelling in opposite directions on either side of it. The other separation zone is marked by the warm front symbol and is more difficult to see since the separation occurs in the vertical. However, the trajectories show that air approaching the southern side of this zone has taken a quite different course from the relatively undisturbed westward flow on its northern side. When it reaches the separation zone, the warm air approaching from the south ascends over the colder flow and then turns sharply to the left to flow parallel to it but at a higher level. The deformation of fluid parcels during the motions depicted in Fig 7 is well illustrated by Fig 8. Here the parcel positions at 144 hours have been joined together in the same order as the initial square grid at 96 hours, using the same convention of cross size to indicate altitude. The stretching out of parcels along the cold front is easily seen but the deformation occurring as parcels rise in the warm front region can

also be discerned. It is interesting to note from this diagram the rapidity with which subsiding parcels behind the cold front have travelled round the south side of the anticyclone and are close to being absorbed in the next depression. Two trajectories are marked in Fig 7a for further study. Profiles of diagnostic quantities following each profile are given in Fig 9. No.1 (Fig 9a) is in region A and is a cold air parcel which starts northwest of the centre and travels southwards behind the cold front. Initially its track is horizontal but towards the end of the period it descends to about 980mb. Its relative vorticity starts at about $3 \times 10^{-5} s^{-1}$ in the region of cyclonic vorticity around the centre. This drops steadily due to compression of vortex lines in the divergent velocity field to end at about the same magnitude of anticyclonic vorticity. The increase in deformation towards the end of the period is due to the parcel approaching the trailing cold front. Temperatures are not available below 950mb since they are defined at mid-levels by the layer thickness and so cannot be plotted for this parcel. However, the initial temperature is $-8^{\circ}C$. By contrast the warm air parcel No.2 (Fig 9b) starts with a temperature of $5^{\circ}C$. It shows substantial ascent reaching 820mb by the end of the period. This parcel is in a convergent velocity field at all times and acquires substantial cyclonic vorticity by stretching. The abrupt change at 132 hours marks the parcel's sharp turn to the left and is marked by an asterisk in Fig 7a.

At 750mb (Fig 10) four regions of flow can be identified although only one of the boundaries shows the characteristics needed to label it as a front. In particular, the boundary between regions A and B

is not a front at this level. It merely marks the trough line at which parcels stop descending. There is some evidence of a zone of confluence further east at which cold air parcels from the west are juxtaposed with warmer air parcels from the east. However, the distinction is poorly marked. By contrast, the vertical separation at the warm front is much clearer here than at the lower level. There are two distinct streams of warm air travelling northwards and ascending over the lower air travelling to the west. The stream nearer to the centre turns to the left round the centre, while the other turns right away from it. The relationship of the final parcel positions to the 1000mb height field is shown in Fig 11. The distortion of the originally square cells is much less than at 950mb. However, the parcels which have risen in the region of the warm front are stretched along a line eastwards from a point just north of the centre, and then curving southwards. The northward displacement reflects the level at which these parcels are being plotted (about 600mb). There is a slight indication of the position of the cold front at the turning point of the southernmost rows of parcels above the surface cold front position. However, no strong deformation is present. Two parcels are marked in Fig 10a for further study and profiles of diagnostic quantities following their motion are given in Fig 12. No.1 is in region B (Fig 12a) and shows marked ascent as it rises over the warm front and turns left. It reaches 580mb by the end of the period with a peak rate of ascent of $1.7\ \mu b\ s^{-1}$ at 136 hours. The velocity field is slightly convergent at first during which time the vorticity reaches $4.2 \times 10^{-5} s^{-1}$. The temperature drops sharply as the parcel ascends, keeping close to the dry adiabat. Calculated values of the temperature fall due to adiabatic ascent are marked on the diagram and verify the conservation of

potential temperature by this parcel. The other parcel (Fig 12b) also shows marked ascent reaching 570mb. Its peak rate of ascent is reached in the middle of the period and reduces nearly to zero by the end. At the same time the velocity field becomes weakly divergent and the very small vorticity becomes anticylonic. These changes are associated with the parcel turning to the right during its ascent at the warm front.

d) Occluding Stage

The final period of analysis is centred on 144 hours with trajectories computed for 48 hours from 120 hours. After 144 hours the low pressure centre becomes stationary and the final stages of the non-linear development occur. Figure 13 is a composite diagram of the main diagnostic fields at this time. The overall height difference has increased to 303m (about 52mb surface pressure) with the low centre having a pressure of about 980mb. The isotherms marked in Fig 13 show that the region of warm air on the east side of the centre has formed a narrow tongue around the north side while cold air from the west has begun to form a tongue round the south side. The cold air incursion is marked by a region of anticyclonic vorticity and descent on the south side of the centre. The maximum cyclonic vorticity occurs at the surface pressure centre and has a value of about $10^{-4}s^{-1}$. There is a secondary maximum along the cold front with values of about $3 \times 10^{-5}s^{-1}$. The eastern end of the main vorticity maximum marks the region of greatest ascent at 550mb. The largest value is about $2\mu bs^{-1}$. These fields may be compared with Fig 10 of Hoskins and West (1979). The height range is again in close agreement. Their temperature pattern shows a rather less developed tongue of warm air round the

north side of the centre and a sharper gradient at the cold front. The main differences, however, are in the magnitudes of the relative vorticity maxima. At the pressure centre they show $3 \times 10^{-4} s^{-1}$ (cf 10^{-4} here) and on the cold front $1.2 \times 10^{-4} s^{-1}$ (cf 0.3×10^{-4} here). The scale of these regions of higher vorticity is, however, comparable with the grid-length of the present model and so it is inevitable that the integration scheme will smooth them out. In particular, the width of the region enclosed by the 0.5 f isopleth on their cold front is much less than a grid-length of the model used here. Other contributions acting in the same way will come from the diffusion terms and from the fact that the 1000mb surface does not form the lower boundary.

Trajectory computations were performed in the same way as for the earlier stages. Figure 14 shows the results for parcels initially at 950mb. The schematic diagram shows a new region E where cold air from the north side of the system is circling round the south side instead of travelling down the cold front. The cold front is more difficult to locate in this region since there is now no difference in flow direction across it, although this characteristic still occurs at greater distances from the centre. However, a distinction can be drawn between the parcels which originated to the right and are ascending as they travel northwards, and those which came from the left and are keeping to a horizontal or slightly descending track. The flow of warm air ahead of the cold front shows marked ascent (up to about 160mb in 48 hours) and the later parcels to reach the warm front show more reluctance to turn left which emphasises the flow separation there. At 750mb (Fig 15), the flow is not greatly different from the mature stage except that where the cold subsiding air has travelled round the south side of the centre, a

meridional structure of a basic state jet, such as that used in the present work, limits the meridional scale of disturbances which again stabilises very long waves. However, for unstable wavelengths it also causes a meridional dependence of the trough and ridge axes which leads to the arrow-head shape in the vorticity field noted in Fig 3c. The energy budget for a growing baroclinic wave can be obtained by suitable averaging of the momentum and thermodynamic equations (eg Holton 1979). For the eddy kinetic energy K' this yields

$$\frac{dK'}{dt} = \gamma \langle \omega' T' \rangle$$

where γ is a constant, the brackets indicate a zonal average and primed quantities are deviations from the zonal average. The equivalent equation for the eddy potential energy P' is

$$\frac{dP'}{dt} = \delta \langle v' T' \rangle - \gamma \langle \omega' T' \rangle$$

where δ is another constant. Thus eddy energy is gained by warm air ($T'>0$) moving north ($v'>0$)and cold air moving south ($T'<0$, $v'<0$), and becomes kinetic energy when warm air ascends ($T'>0$, $\omega'>0$) and cold air descends ($T'<0$, $\omega'<0$). In a baroclinic fluid these processes are accomplished by air parcel trajectories which lie between the isentropes and the geopotentials. This behaviour is well illustrated by Fig 4 where parcels travelling through the system first perform a northward, upward excursion and then a southward, downward one. The constraints on this motion can be seen by analysing the ageostrophic flow (including the vertical motion) forced by the geostrophic motion. Hoskins et al (1978) have developed such a theory in a most elegant way enabling qualitative estimates of the forced circulations to be made in a rigorously based manner and providing a theoretical understanding of quantitative calculations. Their analysis yields an equation for the vertical velocity ($\frac{dz}{dt}$).

recognisable boundary now exists between it and the warm air flow to the east. Vertical motion is substantially greater than in the earlier period and a greater proportion of ascending warm air parcels turn right over the warm front as they reach their maximum altitude near 500mb.

4. DISCUSSION

The first stage of development was labelled the linear stage since the structure of the wave is largely that obtained by linear perturbation analysis. Eady (1949) performed the classical analysis by taking the quasi-geostrophic vorticity equation on an plane and performing a normal mode perturbation analysis about a baroclinic mean state. The resulting eigenvalue problem yielded imaginary phase velocities (and hence instability) for waves longer than a defined minimum. The structure of an unstable wave can be found from the associated eigenfunction and a simplified composite diagram is shown in Fig 16. The dominant characteristic is the westward tilt of the geopotential disturbance with height. The indications of temperature and vertical velocity apply only to the mid-level. The temperature phase lines slope eastward while those of the vertical velocity are almost vertical with a slight westward tilt. Subsequently, authors have investigated the effects of the earth's sphericity and of varying the mean wind profile (e.g. Green 1960, McIntyre 1970, Simmons & Hoskins 1976). The variation of Coriolis acceleration produced by the earth's sphericity was found to stablise very long waves and to destabilise waves shorter than the limit found in Eady's analysis. However, the fastest growing wavelengths were little affected except by a small decrease in phase speed. The

$$N^2 \nabla^2 w + f^2 \frac{\partial^2 w}{\partial z^2} = 2 \nabla \cdot \underset{\sim}{Q}$$

where $$\underset{\sim}{Q} \equiv \left(-\frac{g}{\theta_0} \frac{\partial \underset{\sim}{V}_g}{\partial x} \cdot \nabla \theta, -\frac{g}{\theta_0} \frac{\partial \underset{\sim}{V}_g}{\partial y} \cdot \nabla \theta \right)$$

is a measure of the rate of change of horizontal potential temperature gradient on a fluid particle implied by the geostrophic motion. In order to retain thermal wind balance, the wind shear must change implying the creation of an ageostrophic velocity field. Under simplifying assumptions about vertical structure, they showed that cyclonically curved flow forces ascent ahead and descent behind the trough, and that confluent flow forces ascent on the warm side and descent on the cold side of the jet. Thus, as the thermal pattern around the wave is buckled, the pattern of development in Fig 15 is generated with cyclonic development in the forward part of both regions of strong temperature gradient.

The formation of the fronts is a more complex problem although being related to the general development of the wave. Clearly, the ascent at the warm front and descent behind the cold front are related to the general forcing of vertical motion in these areas. Also, it has been seen that the cold front develops on the south-westward arm of cyclonic vorticity in the linear structure, while the warm front is an extension of the head of the arrowhead shape. Nevertheless, the flow shown in Fig 4 does not contain fronts whereas that in Fig 7 clearly does show them. Principal among the changes that have occurred between these diagrams is the reversal of relative flow on the south side of the centre. Two features of the

system's development are associated with this. The first is that the pressure gradient near the centre has become strong enough to provide the acceleration needed to draw parcels inwards in this manner. The second is that the low level parcels spend an increasing amount of time near the centre during which time they acquire large cyclonic vorticity due to the convergence in that region. After leaving it they travel comparatively rapidly along the cold front and so retain the vorticity until a considerable distance from the centre. The front therefore appears as a concentrated region of cyclonic vorticity. Clearly, this feature, and the warm air flow reversal with which it is associated can only appear below the steering level where the undisturbed flow is to the left. By contrast, parcels entering the warm front region have very little vorticity and acquire it directly as a result of the convergence there. Thus, the warm front appears as a relatively weak feature on the 1000mb vorticity field until a late stage in the development. However, the trajectories indicate that a separation zone exists by the mature stage between the rising parcels coming from the south and the cold air stream from the east. This develops in the region of confluence seen at the linear stage on the northern side of the temperature gradient. The separation appears as a vertical one in which warm air parcels override cold air and then turn to travel parallel to them (Fig 7). Near the steering level some of the rising air moves into increasing pressure gradients at higher levels and accelerates ahead of the system. This can be seen in region C of Fig 10. The parcels in region B ascend into the upper trough which has weak gradients and so the parcels travel, as at lower levels, round the centre. In the last stage of development, the

warm and cold air streams have reached their greatest latitudinal displacement so the system ceases to gain energy. The trajectory diagrams show, however, that considerable vertical motion continues to convert eddy potential energy to eddy kinetic energy. The frontal zones extend further from the centre in this period and become more alike at the two levels. The circulation of cold air round the south side of the centre removes the maximum ascent further from the centre and changes the character of the cold front. The trajectories indicate that relative flow is now parallel on the two sides of the front but with ascent on the east side and descent on the west side. The two streams of air are fed from opposite directions at their southern ends and the warm flow, in particular, is strengthened as it moves north-eastwards (Fig 14).

5. CONCLUSIONS

The developing structure of an ideal baroclinic wave in a forecast model has been described using trajectory techniques. Three stages were analysed and a summary of the relative air flow at each stage is given in Fig 18. At the linear stage, there are no separation zones between different regions of flow. The trajectories are almost horizontal, and at low levels the air is left behind by the system. At the mature stage, the warm air flow on the south side of the centre has been accelerated to the system speed resulting in the formation of two flow discontinuities, a horizontal one at the cold front and a vertical one at the warm front. The final, occluding stage shows cold air trajectories circulating the pressure centre and results in a different structure at the cold front. The flow patterns at the two

levels become very similar at this stage. The second and third stages were compared with equivalent times in the integration reported by Hoskins and West (1979) and qualitative agreement was found. As expected, the geostrophic coordinate transformation used in their model results in less smoothing in the frontal regions and hence in better resolution of the temperature gradients and vorticities. The agreement is sufficiently good for the structural development described in § 3 to serve as a basis for comparison with experiments involving moisture and real initial conditions.

ACKNOWLEDGEMENTS

The work described in this paper was presented as part of a doctoral thesis of Reading University. I am grateful to my supervisors Prof. R P Pearce and Dr A J Gadd for their guidance and support throughout the course of the work. I am also grateful to Prof. B Hoskins, Mr A Gilchrist and Dr K Browning for discussion of the results. Staff of the Forecasting Research Branch of the Met Office provided the initial conditions for the integration. The diagrams were produced with the help of staff of the Data Processing and Central Forecasting Branches and were drawn by the Cartographic Section of the Met Office. I am grateful to the Met Office Typing Pool for preparing the manuscript.

JB

Appendix: Derivation of a vorticity equation in finite differences for the Lax-Wendroff integration scheme.

The analysis is performed on the equation

$$\frac{\partial u}{\partial t} + u\frac{\partial u}{\partial x} + v\frac{\partial u}{\partial y} = 0 \qquad (4)$$

A corresponding result for the v component of the momentum equation is obtained by inspection. The two step Lax-Wendroff integration scheme for Eq 4 may be written

$$u_{n+\frac{1}{2}} = \overline{\overline{u_n}}^{xy} - \frac{\Delta t}{2}\left(\overline{\overline{u_n}}^{xy}\,\overline{\delta_x u_n}^{y} + \overline{\overline{v_n}}^{xy}\,\overline{\delta_y u_n}^{x}\right) \qquad (5)$$

$$u_{n+1} = u_n - \Delta t\left(\overline{\overline{u_{n+\frac{1}{2}}}}^{xy}\,\overline{\delta_x u_{n+\frac{1}{2}}}^{y} + \overline{\overline{v_{n+\frac{1}{2}}}}^{xy}\,\overline{\delta_y u_{n+\frac{1}{2}}}^{x}\right) \qquad (6)$$

where n is the time level and

$$\overline{u}^{x} = \left(u(x,y) + u(x+\Delta x, y)\right)/2$$

$$\delta_x u = \left(u(x+\Delta x, y) - u(x,y)\right)/\Delta x$$

etc

Note that $u_{n+\frac{1}{2}}$ is staggered by half a gridlength in both directions from u_n and u_{n+1}. In principal Eq 5 may be substituted into Eq 6 to give the full equation for u_{n+1}. However the algebra becomes unmanageable. The terms will therefore be treated separately.

Substituting Eq 5 into the first non-linear term of Eq 6 gives

$$\overline{\overline{u_{n+\frac{1}{2}}}}^{xy}\,\overline{\delta_x u_{n+\frac{1}{2}}}^{y} = \left\{\overline{\overline{u}^{x}}^{xy} + \overline{\overline{\delta_x\left[(\overline{u}^{y})^2\right]}}^{xy}\cdot\Delta t + \overline{\left[(\overline{\delta_y\overline{u}^{x}}^{y})\overline{v}^{x} - (\overline{\delta_y\overline{v}^{x}}^{y})\overline{u}^{x} + \delta_y(\overline{\overline{v}^{x}\overline{u}^{x}}^{y})\right]}^{x}\cdot\Delta t\right\} \times$$

$$\times\left\{\overline{\overline{\delta_x\overline{u}^{x}}^{xy}} + \overline{\delta_x\delta_x\left(\overline{u}^{y}\right)^2}^{y}\cdot\frac{\Delta t}{2} + \delta_x\left[(\overline{\delta_y\overline{u}^{x}}^{y})\overline{v}^{x} - (\overline{\delta_y\overline{v}^{x}}^{y})\overline{u}^{x} + \delta_y(\overline{\overline{v}^{x}\overline{u}^{x}}^{y})\right]\cdot\Delta t\right\} \qquad (7)$$

Consistent with the order of accuracy of the scheme, terms of second and higher order in Δt are ignored giving

$$\overline{\overline{u_{n+\frac{1}{2}}}}^{xy}\,\overline{\delta_x u_{n+\frac{1}{2}}}^{y} = \overline{\overline{u_n}^{x}}^{xy}\,\delta_x\overline{\overline{u_n}^{x}}^{xy} + O(\Delta t) \qquad (8)$$

The other term can be obtained in a similar fashion to give

$$\delta_t u = -\overline{\overline{u}^{x}}^{xy}\,\delta_x\overline{\overline{u}^{x}}^{xy} - \overline{\overline{v}^{x}}^{xy}\,\delta_y\overline{\overline{u}^{x}}^{xy} + O(\Delta t) \qquad (9)$$

By inspection it can be shown that the v component of the momentum equation satisfies the relation

$$\delta_t v = -\overline{u}^{xyt}\,\delta_x \overline{v}^{xyt} - \overline{v}^{xyt}\,\delta_y \overline{v}^{xyt} + O(\Delta t) \qquad (10)$$

In order to form the vorticity equation these equations must be differentiated and then subtracted. From the resulting expression the terms corresponding to the total derivative of vorticity may be extracted. The form of these terms is determined to maintain consistency with the advection terms in Eqs 9,10. Thus

$$u\frac{\partial}{\partial x}\left(\frac{\partial u}{\partial y}\right) \equiv \overline{\overline{u}^{xyt}\,\delta_x \delta_y \overline{u}^{xyt}}^{x} \qquad (11)$$

The remaining terms are those associated with the stretching term of the vorticity equation and have the form

$$\mathcal{SD} \equiv \overline{\delta_x \overline{v}^{xyt}\left(\delta_x \overline{u}^{xyt} + \delta_y \overline{v}^{xyt}\right)}^{y} - \overline{\delta_y \overline{u}^{xyt}\left(\delta_x \overline{u}^{xyt} + \delta_y \overline{v}^{xyt}\right)}^{x} \qquad (12)$$

which is very close to $\mathcal{S}_o \mathcal{D}_o$ where $\mathcal{S}_o$ and $\mathcal{D}_o$ are the simplest finite difference forms. This is equivalent to application of a nine-point smoothing operator to each field separately.

REFERENCES

Bjerknes, J 1918 On the structure of moving cyclones. Geofys.Publik.Norske Videnskans - Akad. Oslo 1 No 2.

Bjerknes, J and Solberg, H 1922 Life cycle of cyclones and the polar front theory of atmospheric circulation. Geofys.Publik.Norske Videnskans - Akad. Oslo 3 No.1 pp 1-18.

Browning, K A and Harrold, T W 1969 Air motion and precipitation growth in a wave depression. Quart.J.Roy.Met S,95 pp 288-309.

Burridge, D M and Gadd, A J 1977 The Meteorological Office operational 10-level numerical weather prediction model (December 1975). Sci.Pap. Met O No.34 HMSO London.

Charney, J G 1947 The dynamics of long waves in a baroclinic westerly current J.Met 4 pp 135-163.

Danielson, E F 1961 Trajectories: Isobaric, Isentropic and Actual. J.Met.18 pp 479-486.

Djuric, D 1961 On the accuracy of air trajectory computations. J.Met.18 pp 597-605.

Eady, E.T. 1949 Long waves and Cyclone waves. Tellus 1 pp 33-52.

Gadd, A.J. 1978a A split explicit integration scheme for numerical weather prediction. Quart.J.Roy.Met S. 104 pp 569-582.

Gadd, A.J. 1978b A numerical advection scheme with small phase errors. Quart.J.Roy.Met.S 104 pp 583-594.

Gadd, A.J. 1980 Two refinements of the split explicit integration scheme. Quart.J.Roy.Met.S 106 pp 215-220.

Gilchrist, A. 1971 An example of synoptic development in a general circulation model. Quart.J.Roy.Met.S 97 pp 340-347.

Golding, B.W. 1981 Diagnostic studies of mid-latitude depressions. Ph.D thesis University of Reading.

Green, J.S.A. 1960 A problem in baroclinic stability. Quart.J.Roy.Met.S.86 pp 237-251.

Green, J.S.A. Ludlam, F.H. and McIlveen, J.F.R. 1966 Isentropic relative-flow analysis and the parcel theory. Quart.J.Roy.Met.S.92 pp 210-219.

Holton, J.R. 1979 An introduction to dynamic meteorology. Int.Geoph.Ser.Vol.23, Academic Press, New York.

Hoskins, B.J. 1975 The geostrophic momentum approximation and the semi-geostrophic equations. J.Atmos.Sci.32 pp 233-242.

Hoskins, B.J. and Bretherton, F.P. 1972 Atmospheric frontogenesis models: mathematical formulation and solution. J.Atmos.Sci.29 pp 11-37.

Hoskins, B.J. and West, N.V. 1979 Baroclinic waves and frontogenesis. Part II Uniform potential vorticity jet flows - cold and warm fronts. J.Atmos.Sci.36 pp 1663-1680.

Hoskins, B.J. Draghici, I and Davies, H.C. 1978 A new look at the ω - equation. Quart.J.Roy.Met.S. 104 pp 31-38.

McIntyre, M.E. 1970 On the non-separable baroclinic parallel flow instability problem. J.Fluid Mech.40 pp 273-306.

Mudrick, S.E. 1974 A numerical study of frontogenesis. J.Atmos.Sci.31 pp 869-892.

Pedlosky, J. 1970 Finite amplitude baroclinic waves. J.Atmos.Sci.27 pp 15-30.

Simmons, A.J. and Hoskins, B.J. 1976 Baroclinic instability on the sphere: normal modes of the primitive and quasi-geostrophic equations. J.Atmos.Sci.33 pp 1454-1477.

LIST OF FIGURES.

Fig 1 Idealised schematics of a mature depression a) 950mb b) 750mb

Fig 2 Profiles of the basic state jet a) latitude cross section at 200mb b) Vertical cross section near $45^{\circ}N$

Fig 3 72 hour forecast fields a) 1000mb height in gpm b) 500mb height in gpm c) 1000mb relative vorticity in $s^{-1} \times 10^{5}$ d) 550mb vertical velocity in $\mu b\, s^{-1}$

Fig 4 Diagnosed trajectories for 48-96 hours for parcels initially at 950mb a) computed tracks b) schematic interpretation

Fig 5 Diagnosed trajectories for 48-96 hours for parcels initially at 750mb a) computed tracks b) schematic interpretation

Fig 6 120 hour forecast fields a) 1000mb height in gpm b) 500mb height in gpm c) 1000mb relative vorticity in $s^{-1} \times 10^{5}$ d) 550mb vertical velocity in $\mu b\, s^{-1}$ e) 950mb temperature in K f) composite diagram

Fig 7 Diagnosed trajectories for 96-144 hours for parcels initially at 950mb a) selection of computed tracks b) schematic interpretation

Fig 8 Final positions of the grid of air parcels initially at 950mb superimposed on the 144 hour forecast of 1000mb height

Fig 9 Profiles of diagnostic quantities following parcels in Fig 7 a) No.1 b) No.2

Fig 10 Diagnosed trajectories for 96-144 hours for parcels initially at 750mb a) selection of computed tracks b) schematic interpretation

Fig 11 Final positions of the grid of air parcel trajectories initially at 750mb superimposed on the 144 hour forecast of 1000mb height

Fig 12 Profiles of diagnostic quantities following parcels in Fig 10 a) No.1 b) No.2

Fig 13 Composite diagram of the low pressure centre at 144 hours

Fig 14 Diagnosed trajectories for 120-168 hours for parcels initially at 950mb a) selection of computed tracks b) schematic interpretation

Fig 15 Diagnosed trajectories for 120-168 hours for parcels initially at 750mb a) selection of computed tracks b) schematic interpretation

Fig 16 Simplified structure of an unstable baroclinic wave showing phase relationships between the geopotential, temperature and vertical motion

Fig 17 Development areas predicted by simple application of Q-theory to the thermal structure of a developing depression

Fig 18 Summary of development of relative air flow in a baroclinic wave

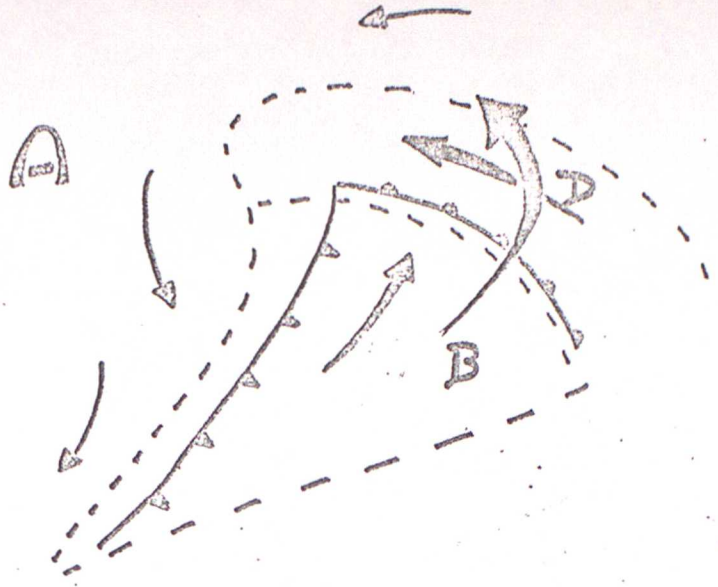

a)

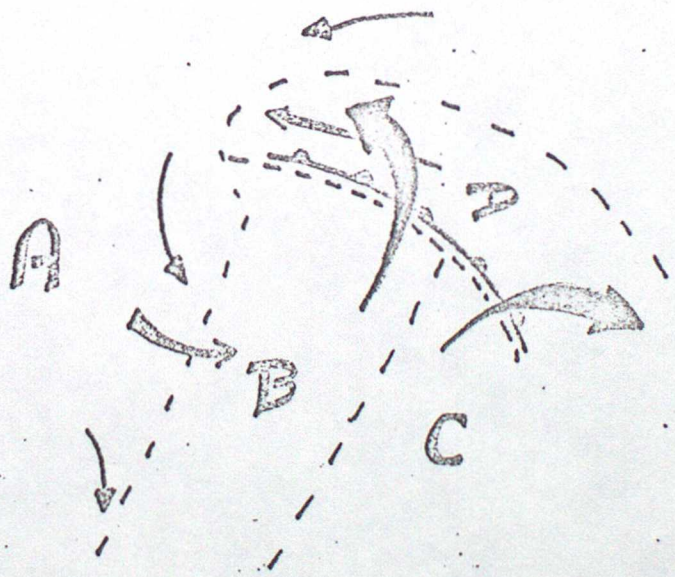

b)

Fig 1

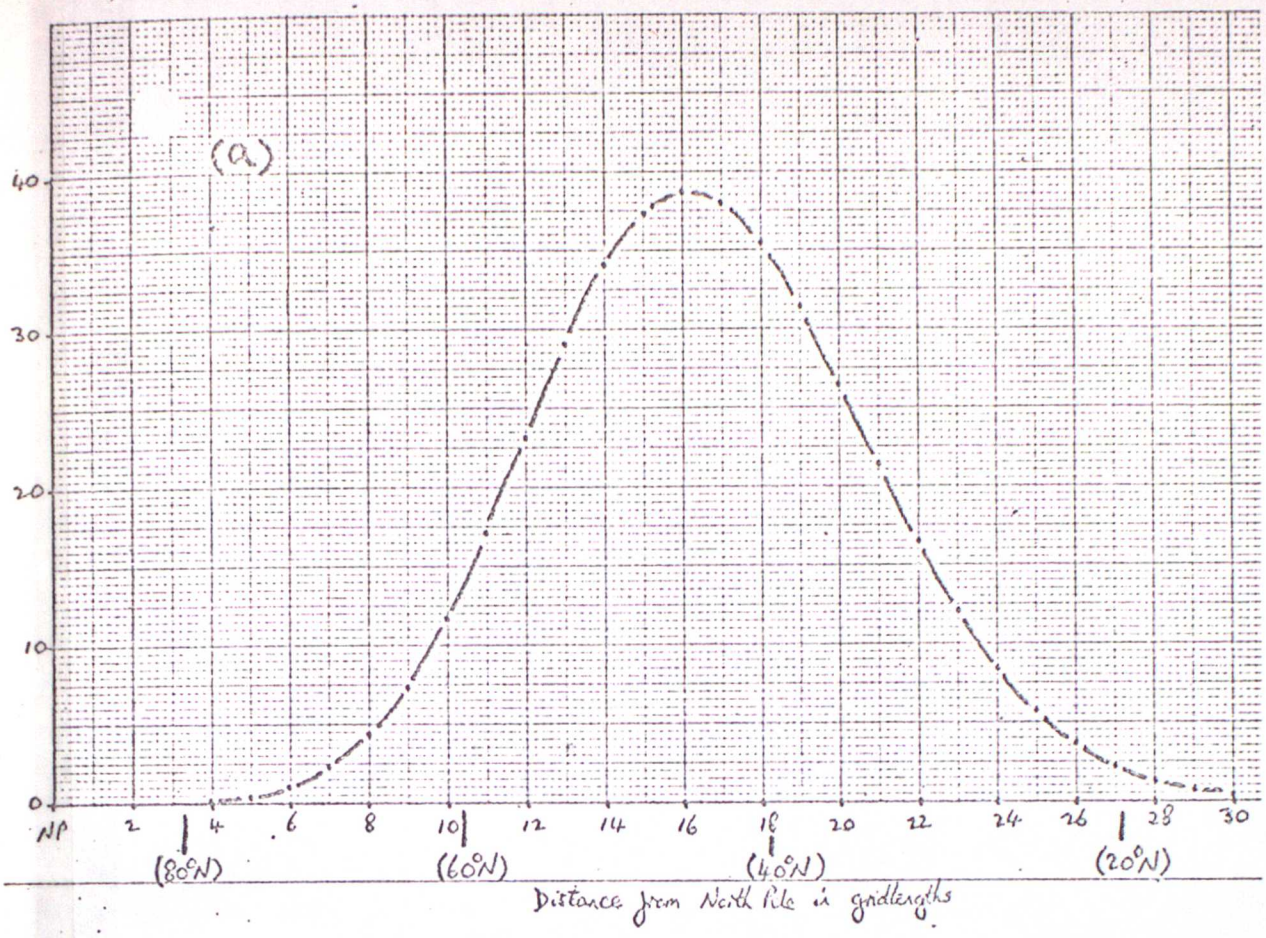
(a)
40
30
20
10
0
NP
2
4
6
8
10
12
14
16
18
20
22
24
26
28
30
(80°N)
(60°N)
(40°N)
(20°N)
Distance from North Pole in gridlengths

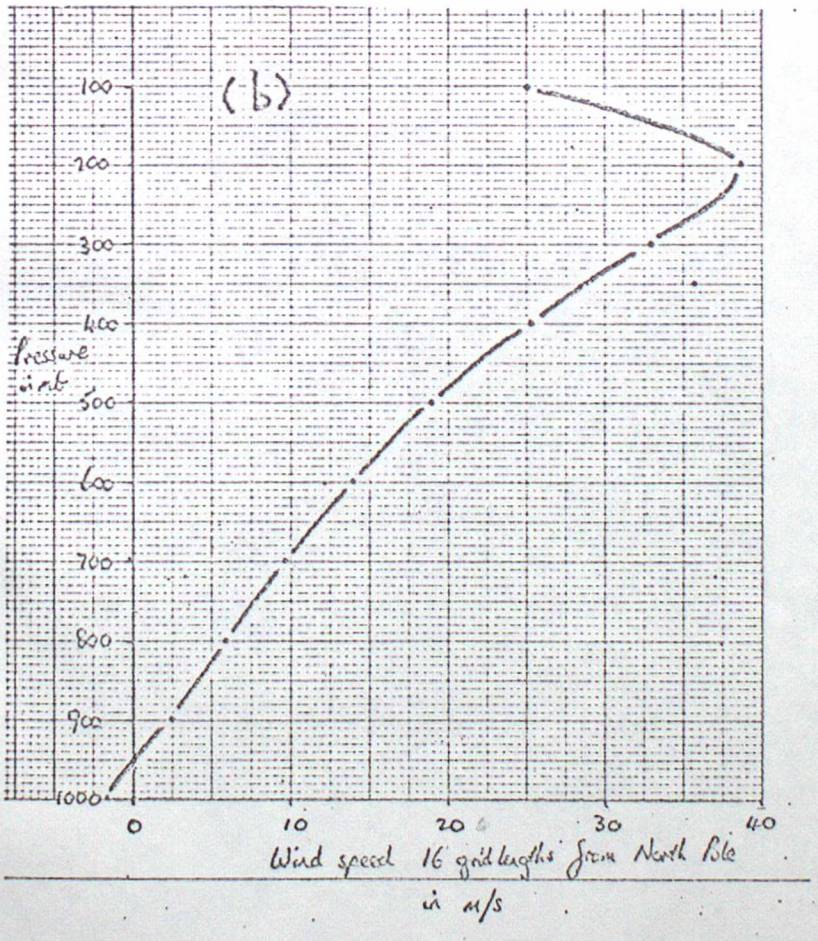
(b)
100
200
300
400
500
600
700
800
900
1000
Pressure in mb
0
10
20
30
40
Wind speed 16 gridlengths from North Pole in m/s

Fig 2

a)

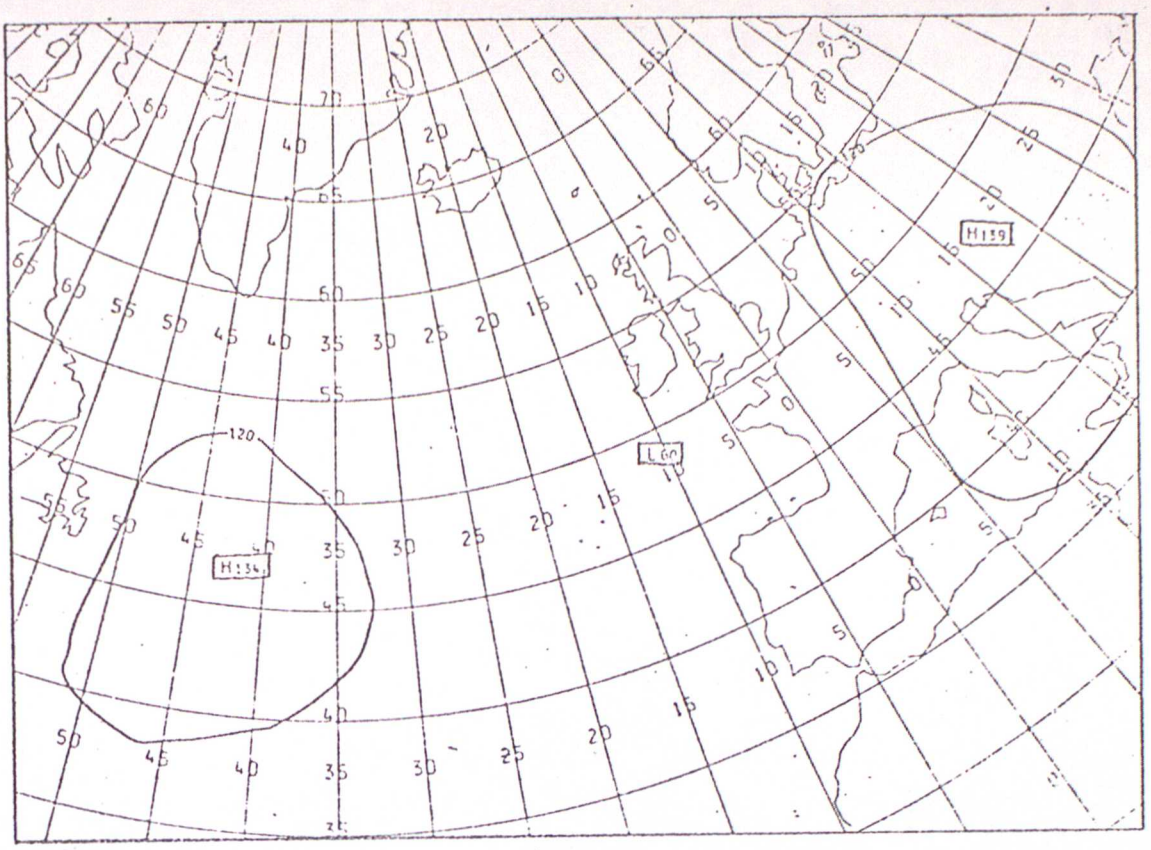

b)

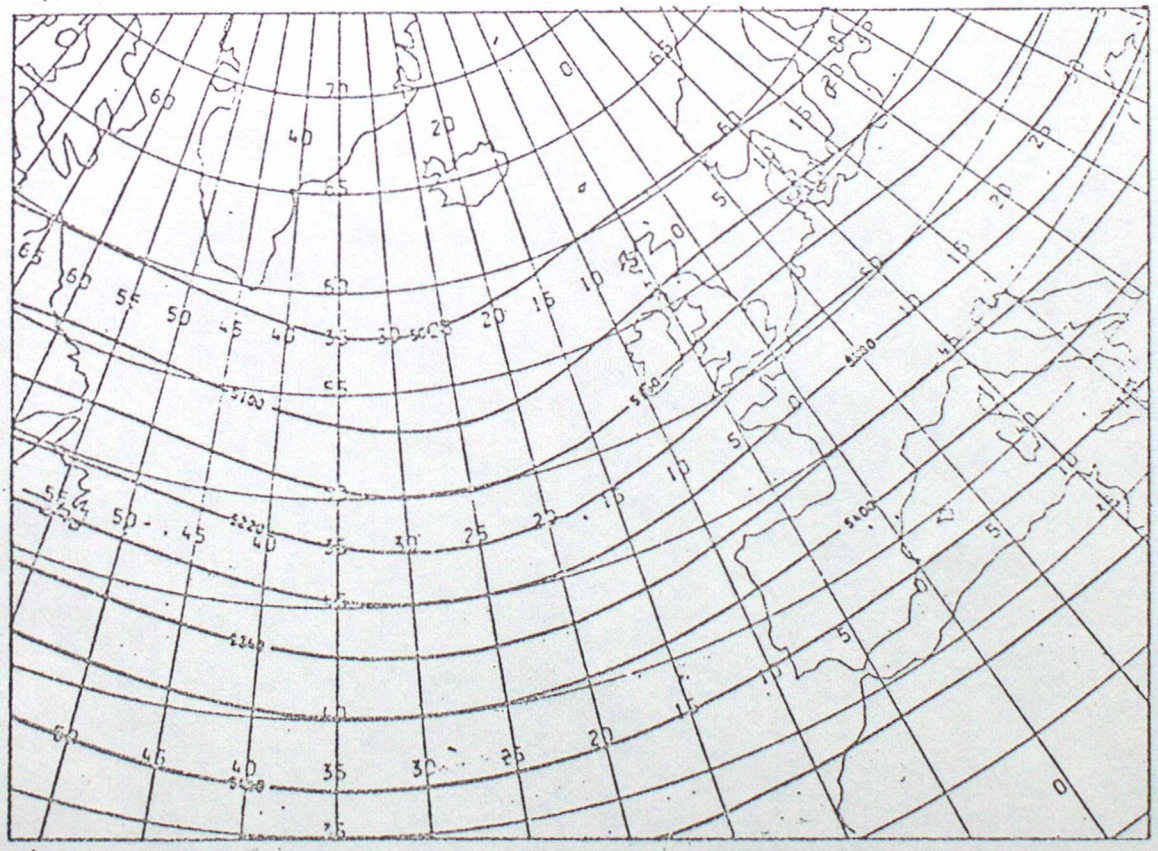

Fig 3

c)

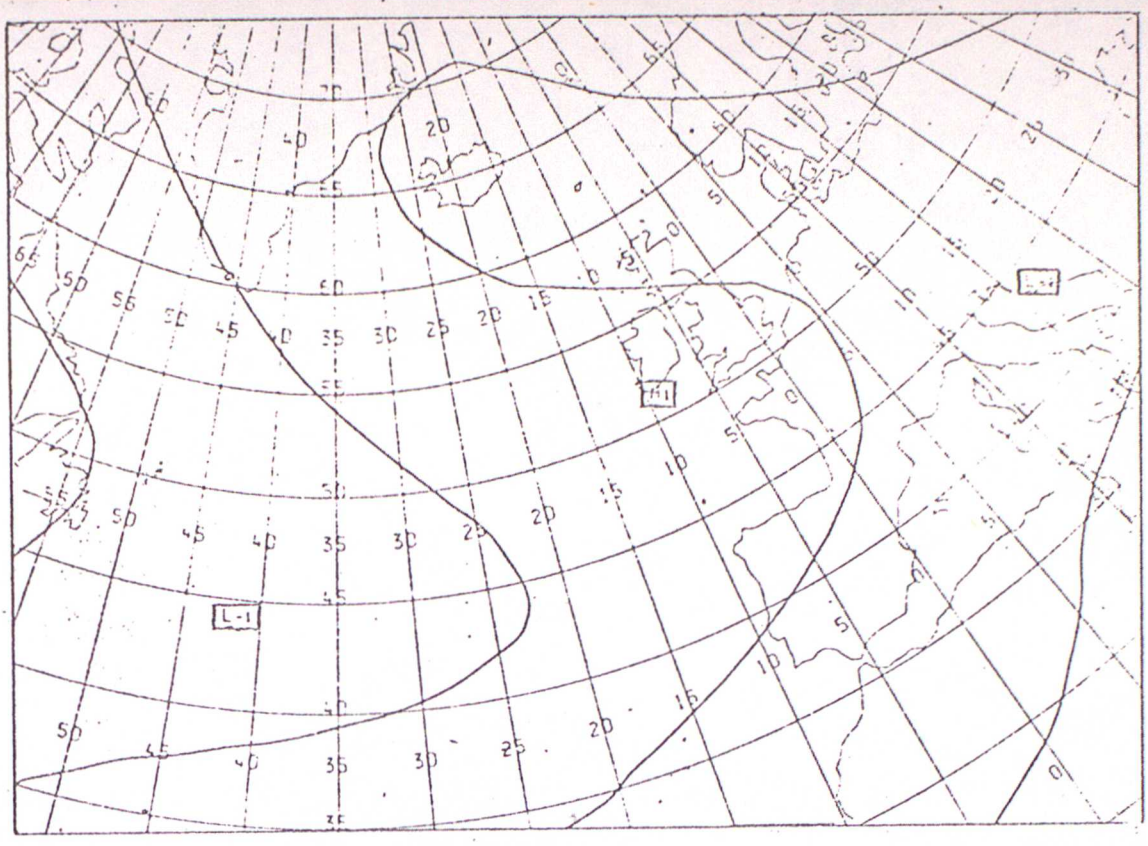

d)

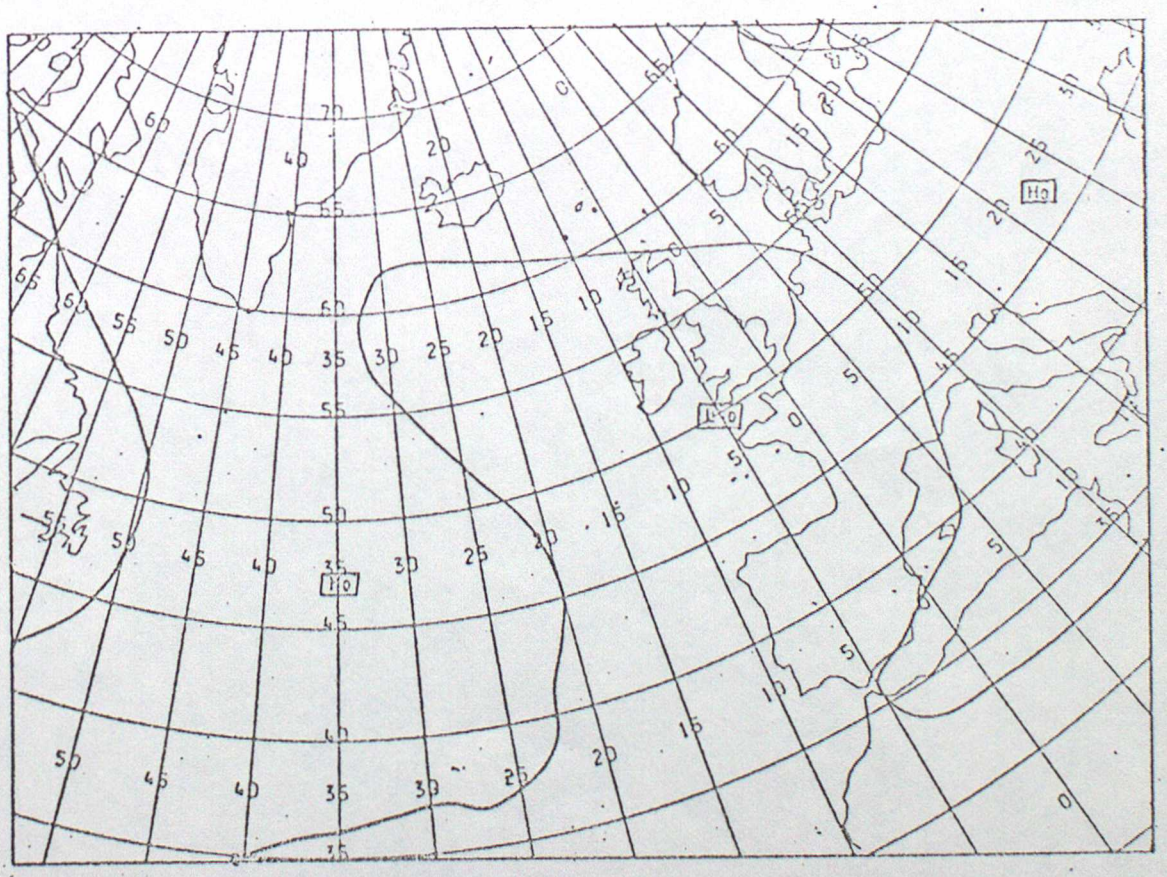

Fig 3

SIZE OF CROSS AT 950mb.

a)

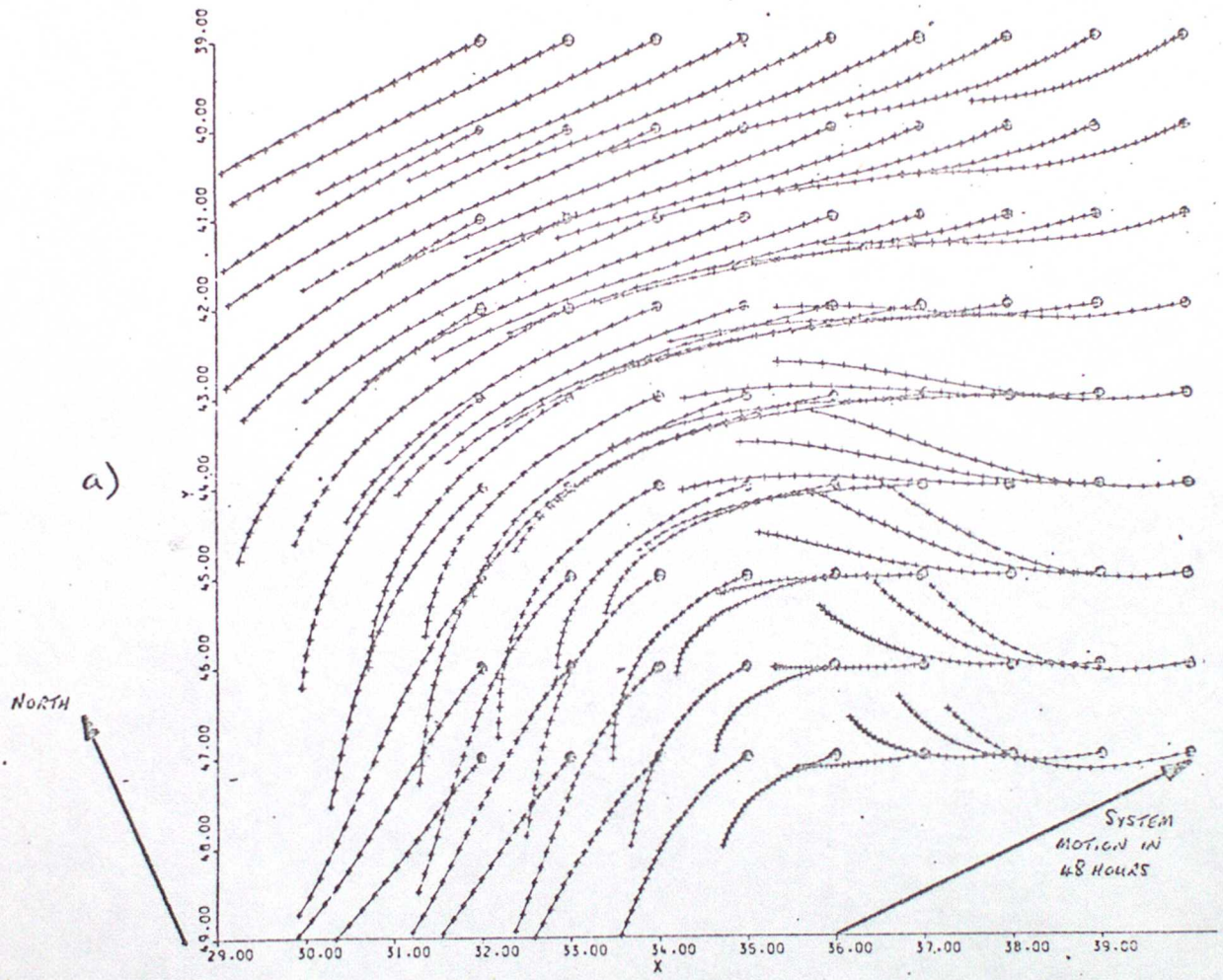

b)

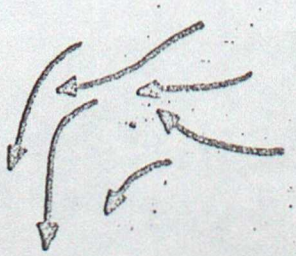

Fig 4

SIZE OF CROSS AT 750 mb.

a)

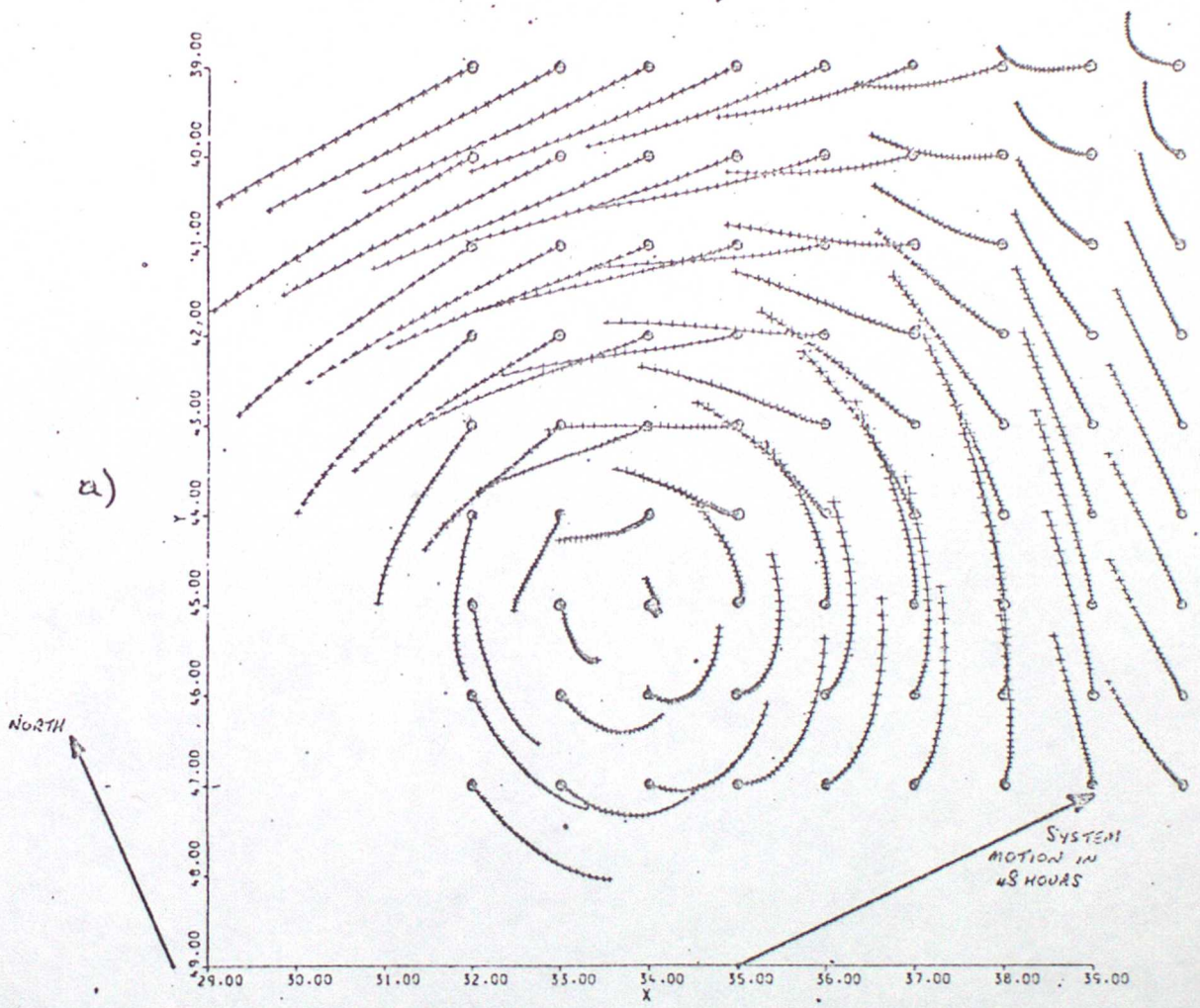

b)

Fig 5

a)

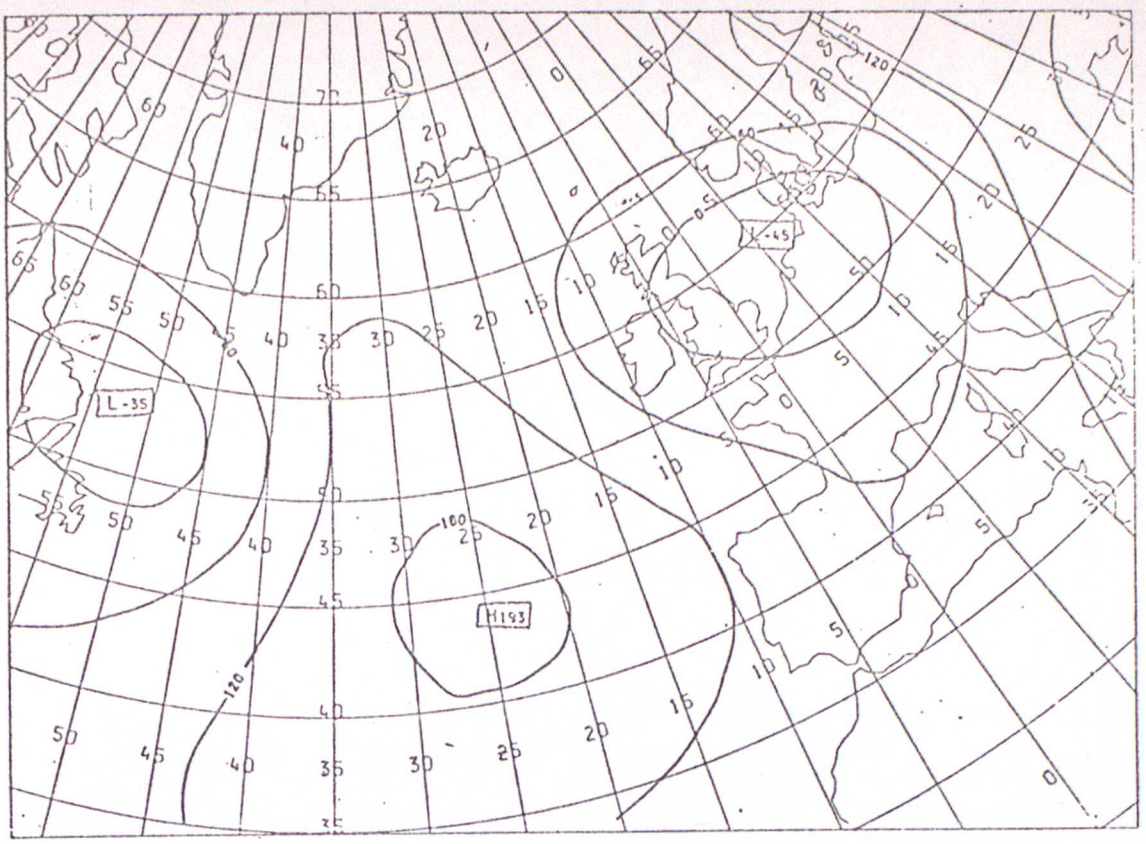

b)

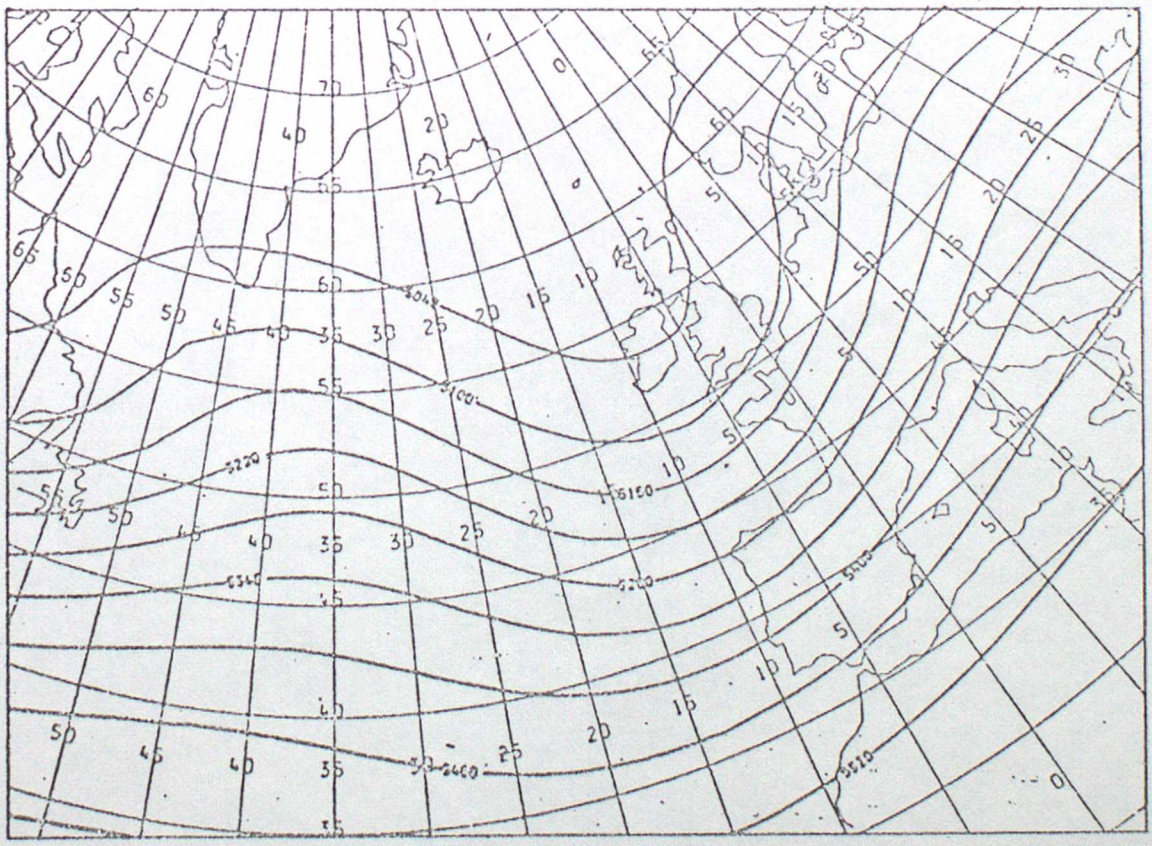

Fig 6

e)

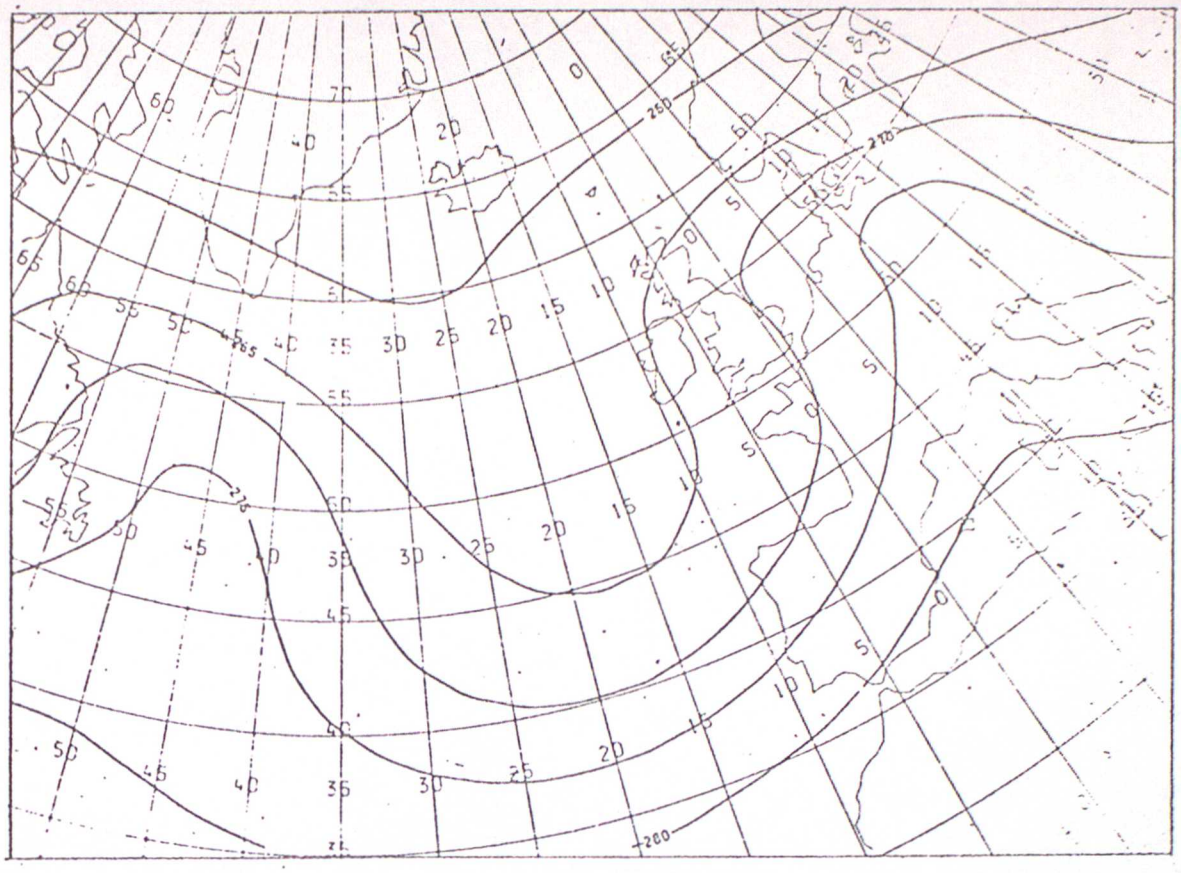

f)

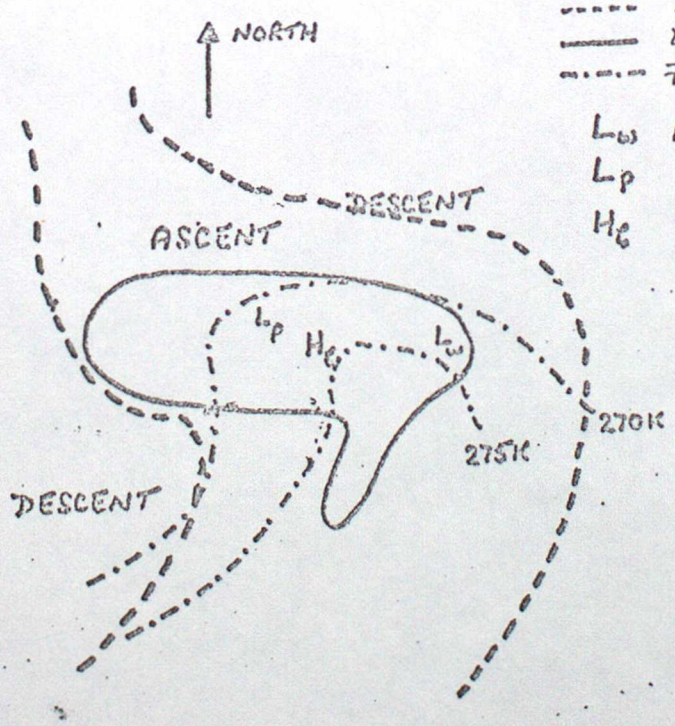

KEY

- ----- $\omega_{850} = 0$
- ——— $\zeta_{1000} = 2\times10^{-5}s^{-1}$
- -·-·- $\bar{T}$ = 270K/275K (900-1000mb mean)
- L_ω Position of MAX ASCENT
- L_p " " MIN PRESSURE
- H_ζ " " MAX VORTICITY

Fig 6

c)

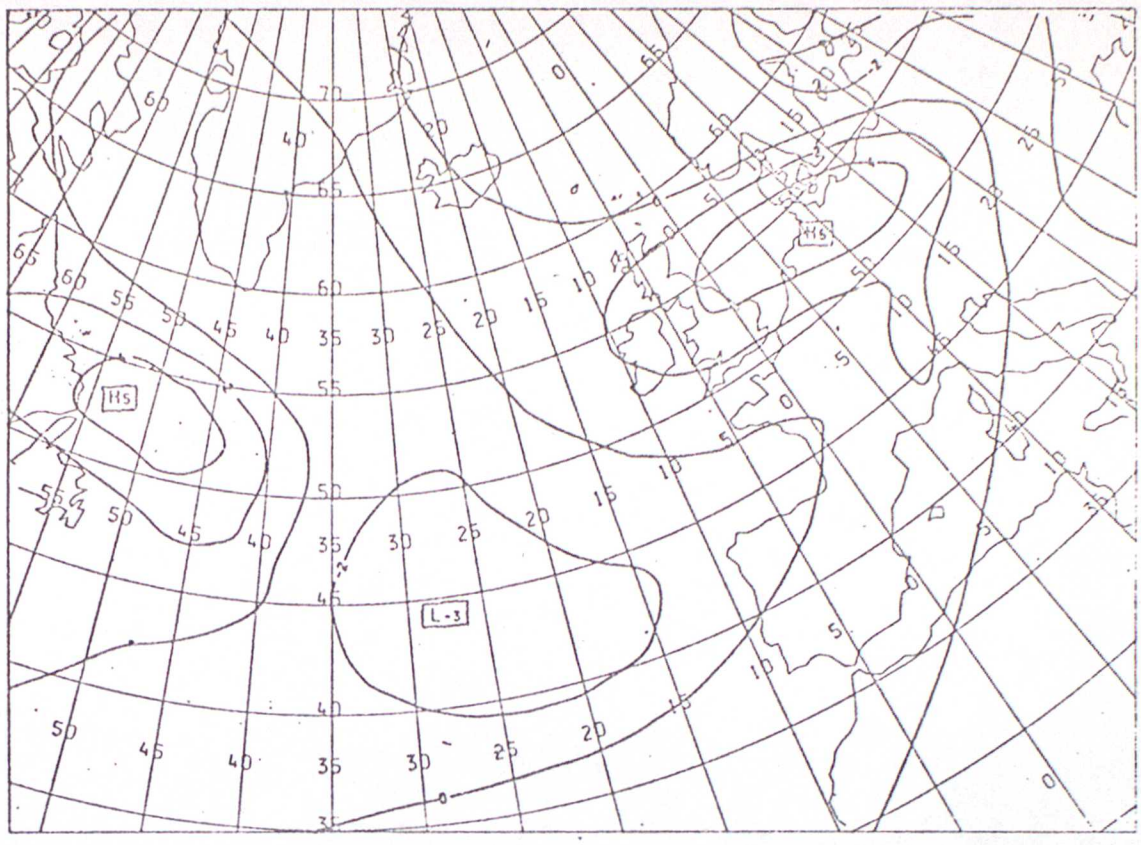

d)

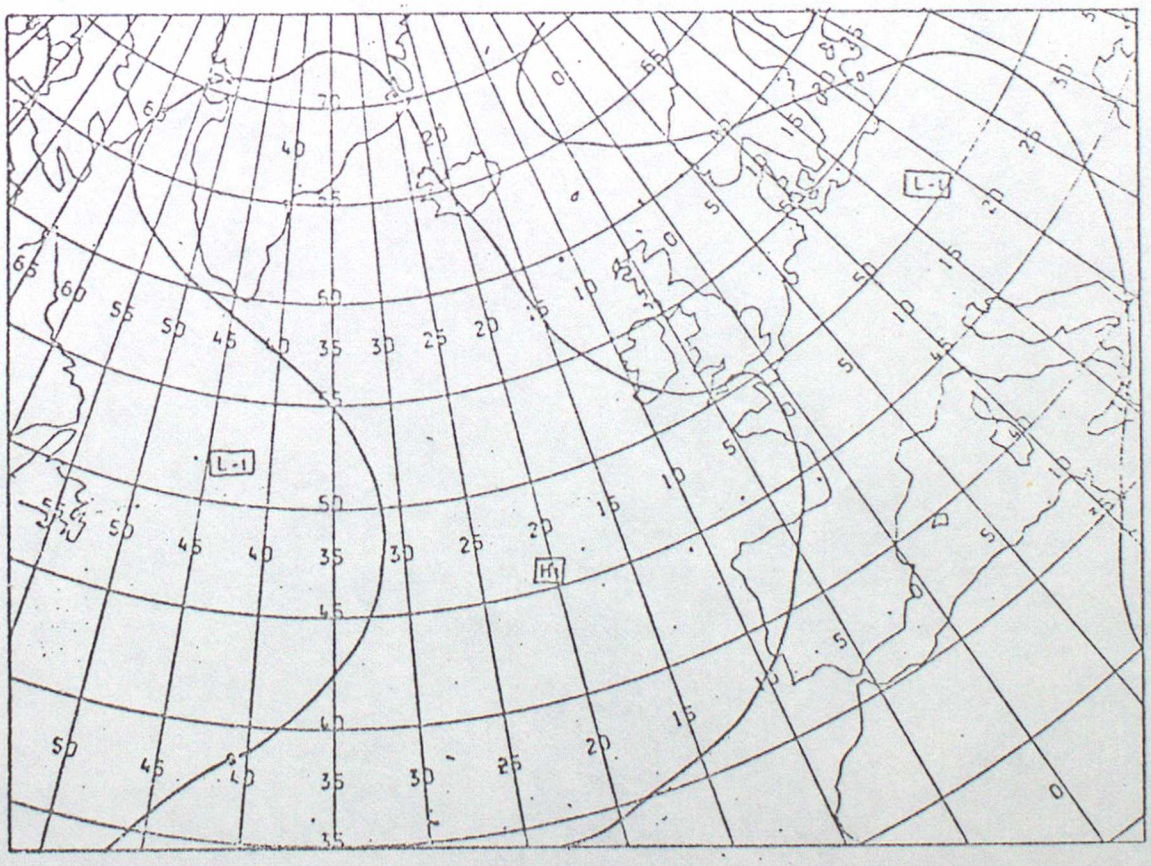

Fig 6

SIZE OF CROSS AT 950mb .

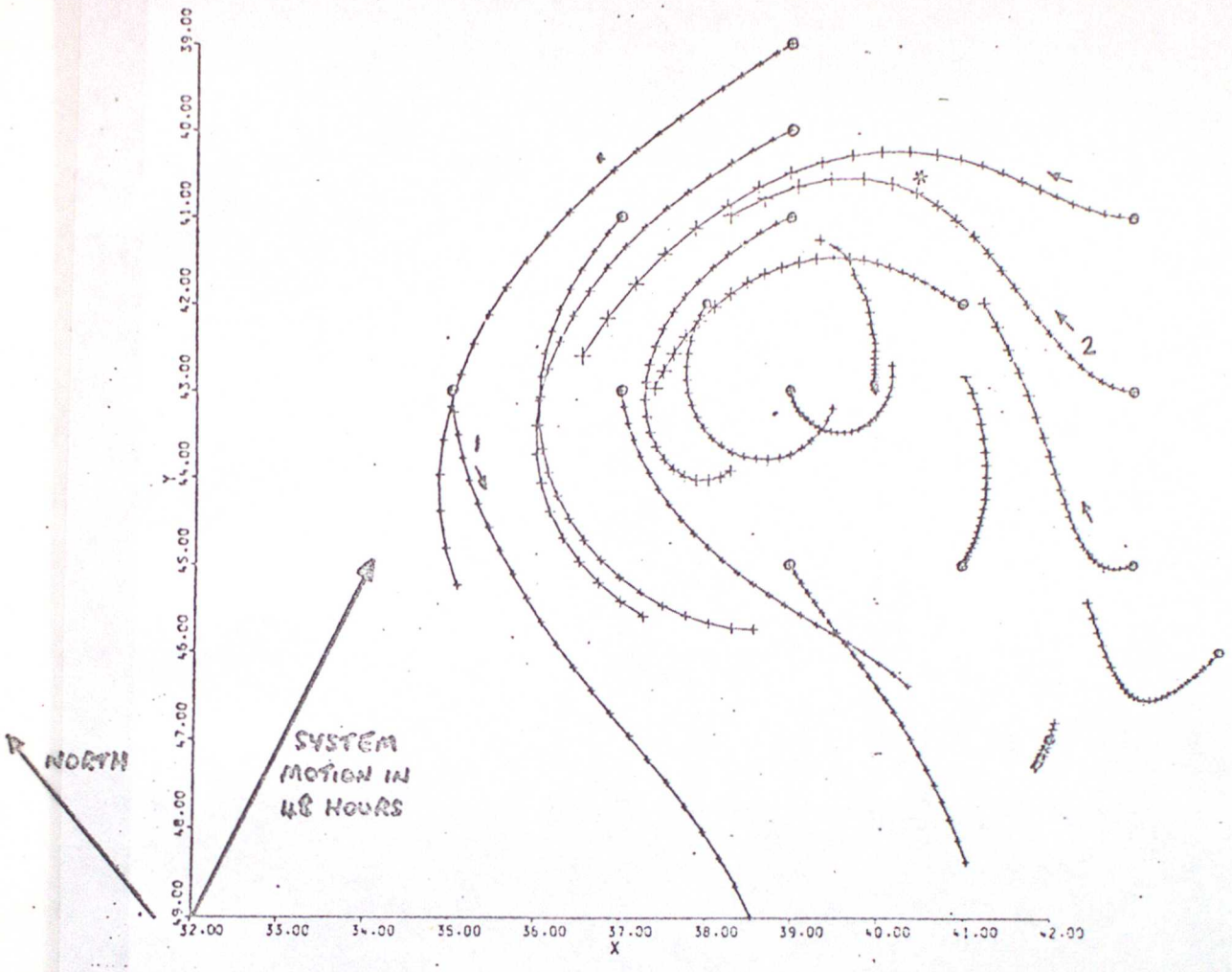

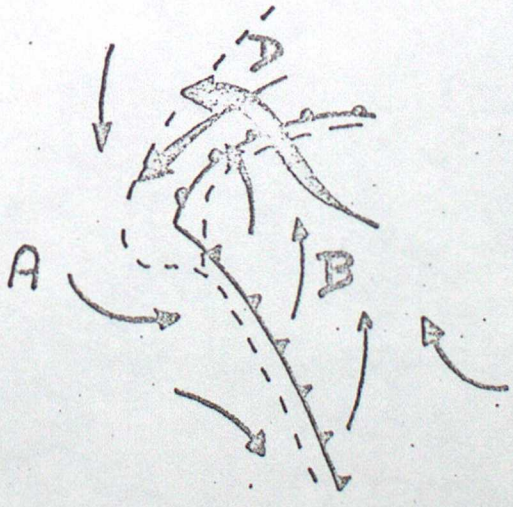

Fig 7

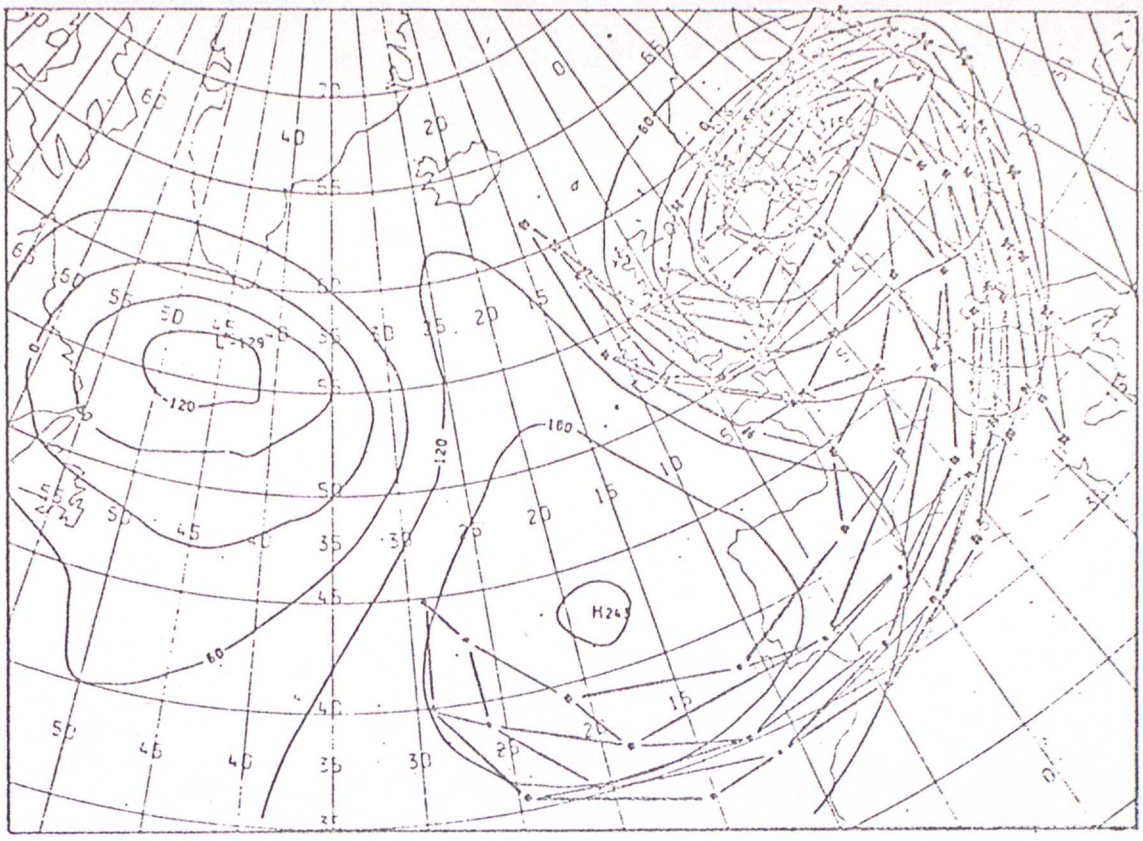

Fig 8

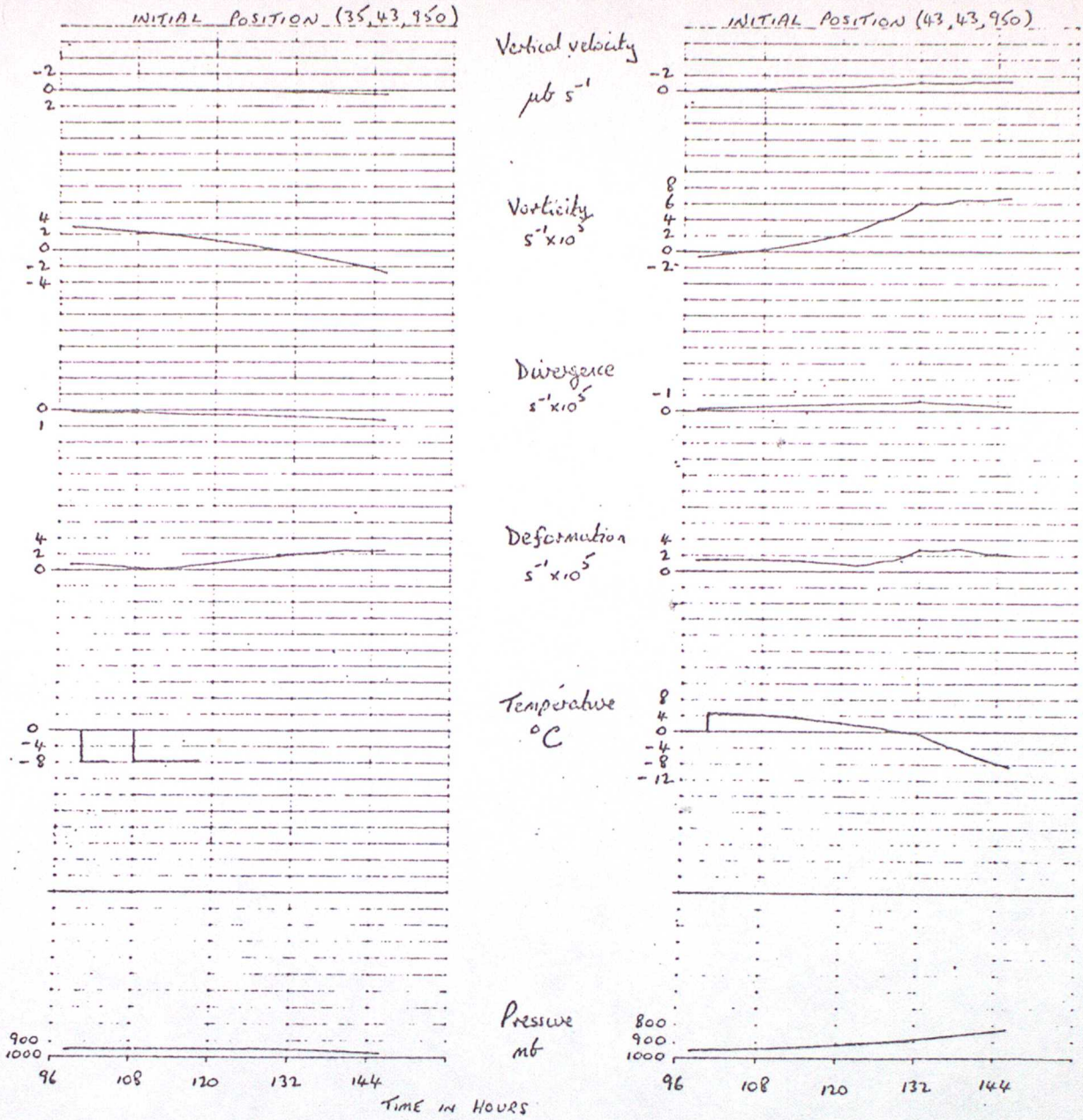
INITIAL POSITION (35, 43, 950)
INITIAL POSITION (43, 43, 950)
Vertical velocity
μb s⁻¹
Vorticity
s⁻¹ x 10⁵
Divergence
s⁻¹ x 10⁵
Deformation
s⁻¹ x 10⁵
Temperature
°C
Pressure
mb
-2
0
2
4
2
0
-2
-4
0
1
4
2
0
0
-4
-8
900
1000
8
6
4
2
0
-2
-1
0
4
2
0
8
4
0
-4
-8
-12
800
900
1000
96
108
120
132
144
TIME IN HOURS
a)
b)

Fig. 9

SIZE OF CROSS AT 750mb.

a)

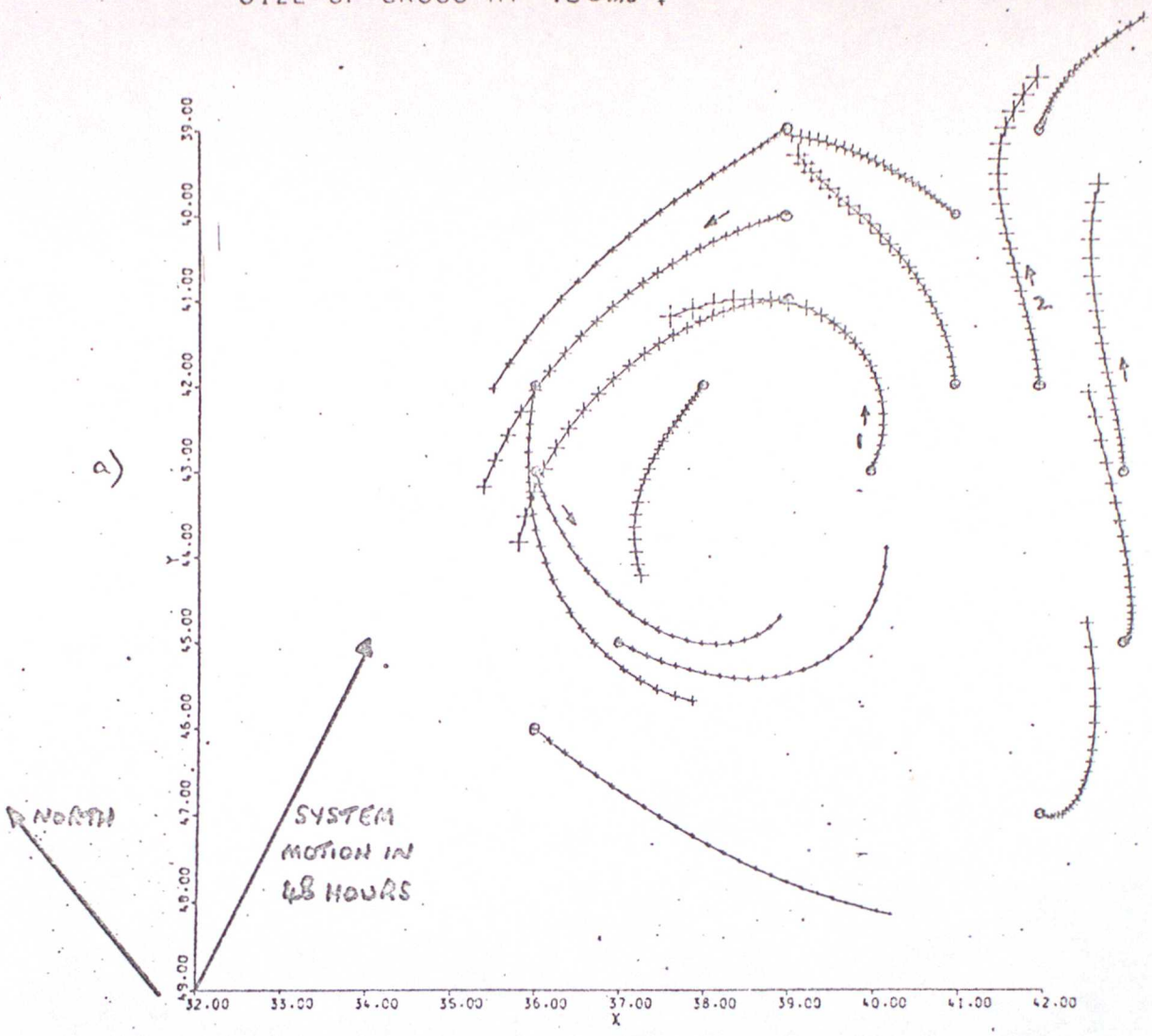

b)

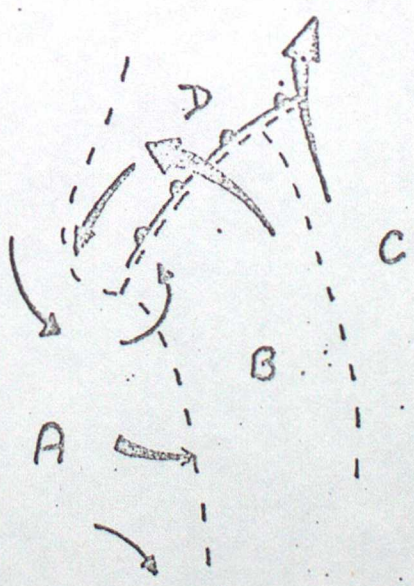

Fig 10

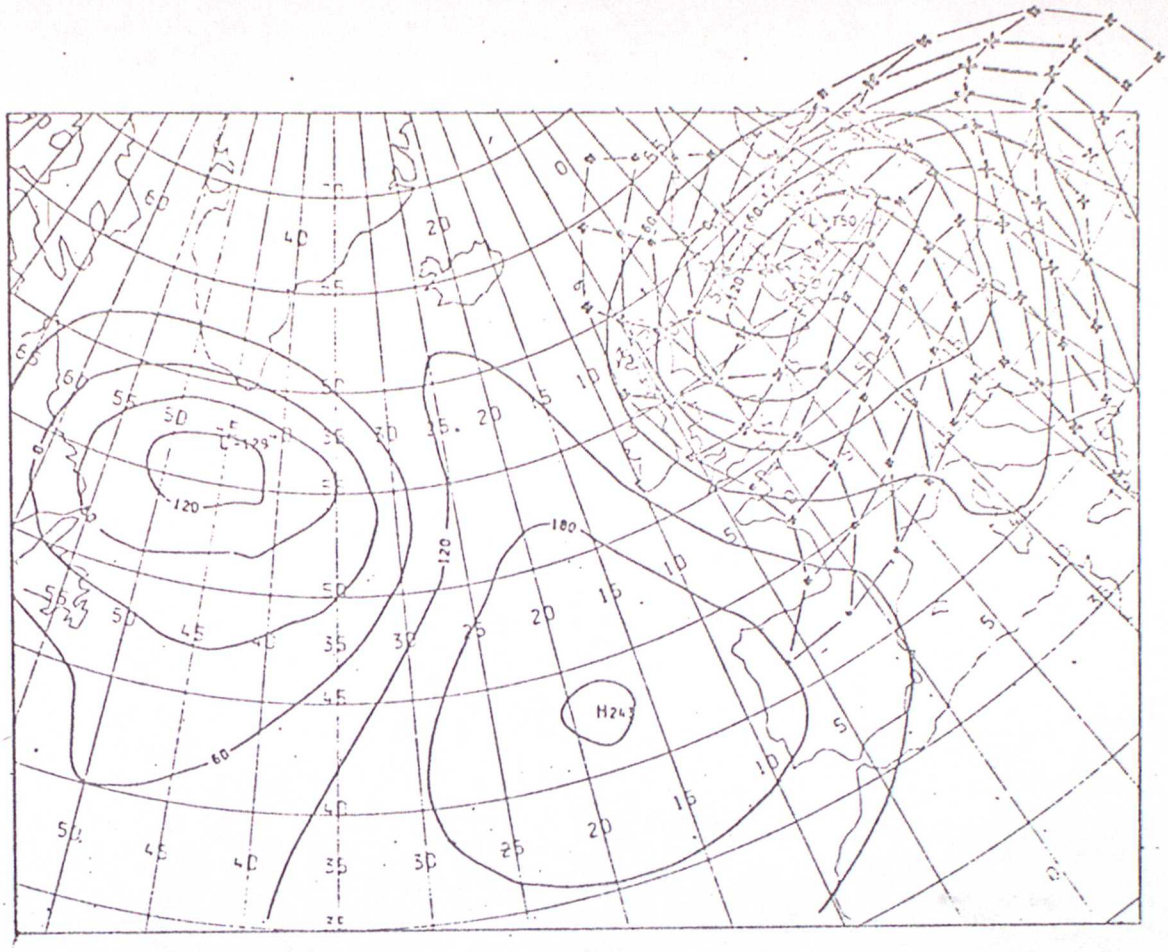

Fig. 11

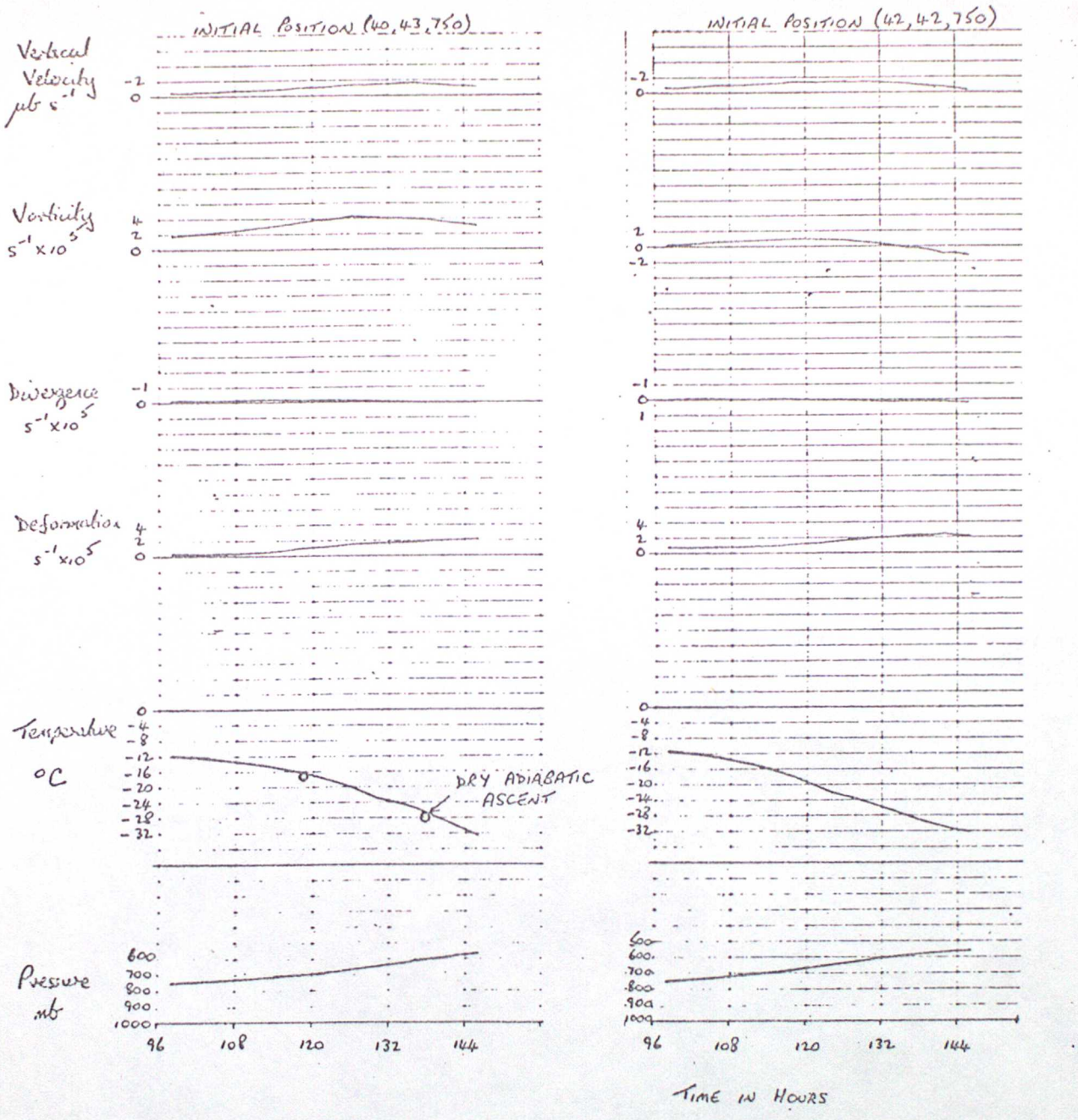
INITIAL POSITION (40, 43, 750)
INITIAL POSITION (42, 42, 750)
Vertical Velocity μb s⁻¹
Vorticity s⁻¹ x10⁵
Divergence s⁻¹ x10⁵
Deformation s⁻¹ x10⁵
Temperature °C
DRY ADIABATIC ASCENT
Pressure mb
96
108
120
132
144
TIME IN HOURS
a)
b)

Fig 12

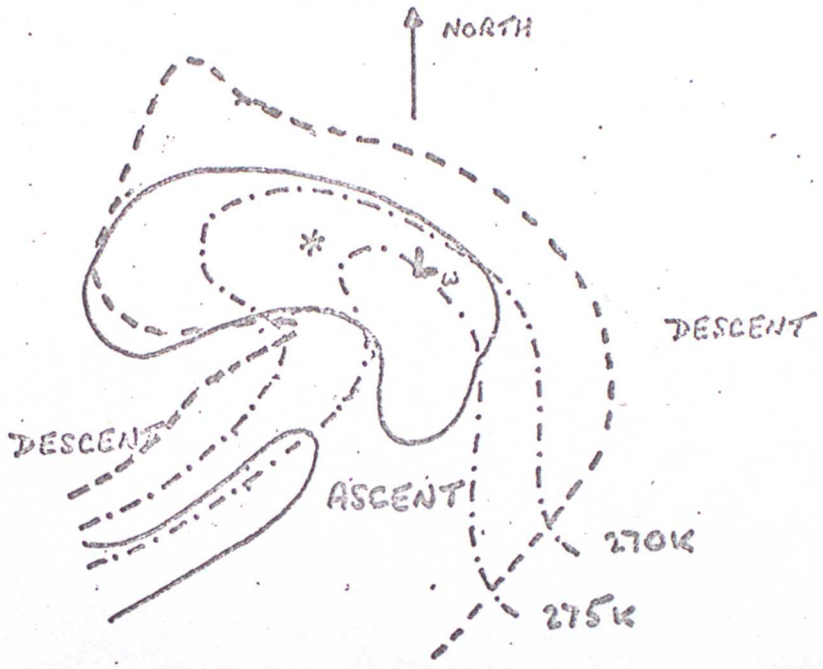

KEY

---- $\omega_{850} = 0$

——— $\zeta_{1000} = 2 \times 10^{-5} s^{-1}$

-·-·- $\bar{T} = 270/275K$
(900-1000mb mean)

* Location of MAX VORTICITY, MIN PRESSURE

L_ω Location of MAX ASCENT

Fig B

SIZE OF CROSS AT 950mb .

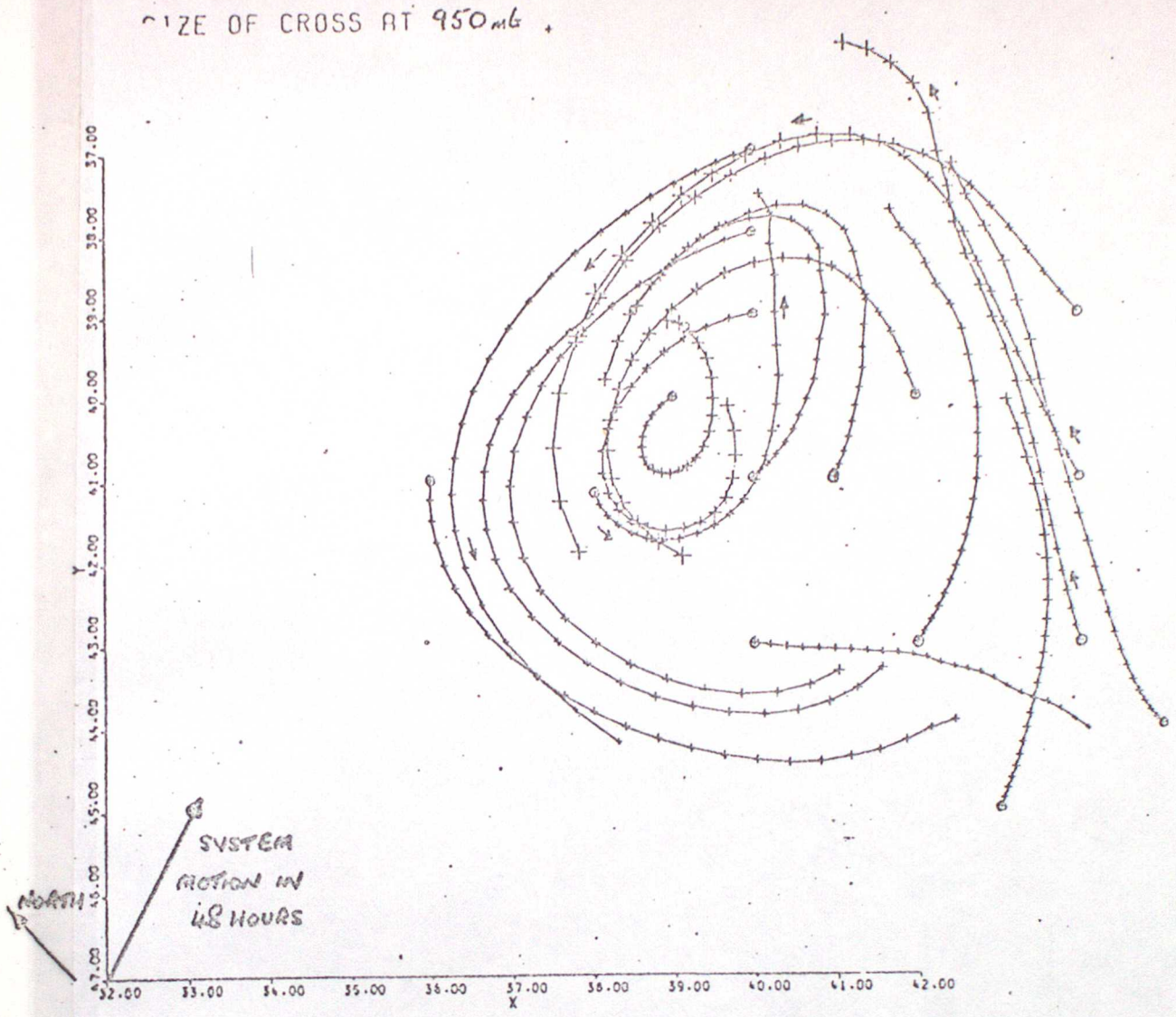

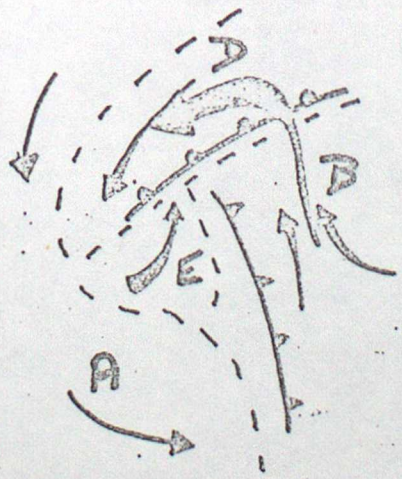

Fig 14

SIZE OF CROSS AT 750mb.

a)

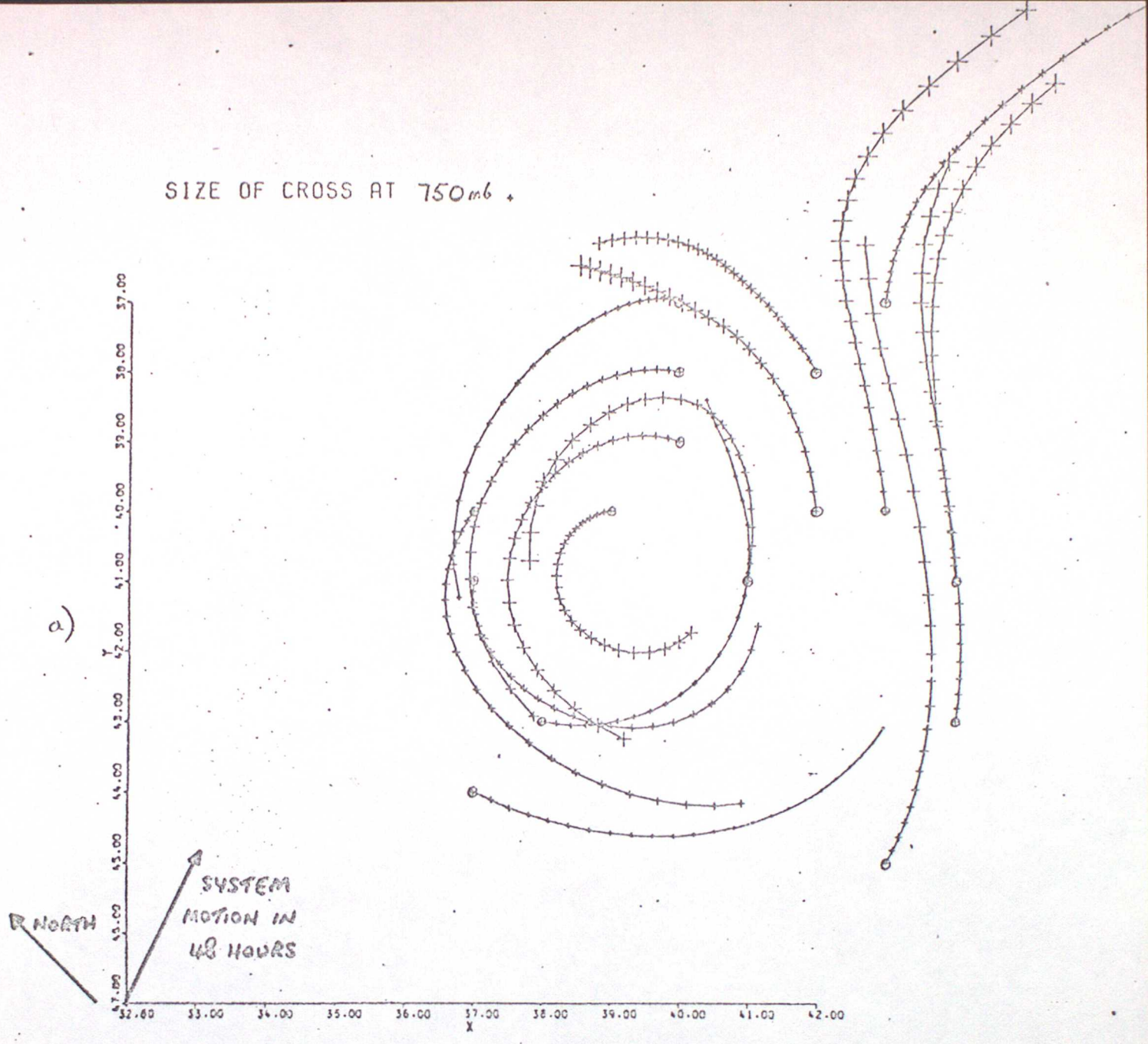

b)

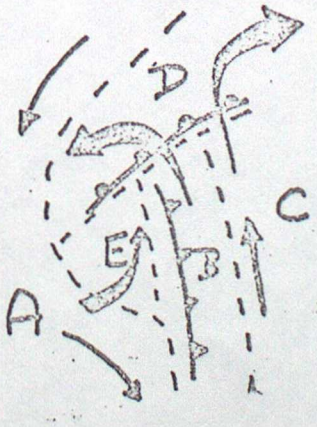

Fig 13

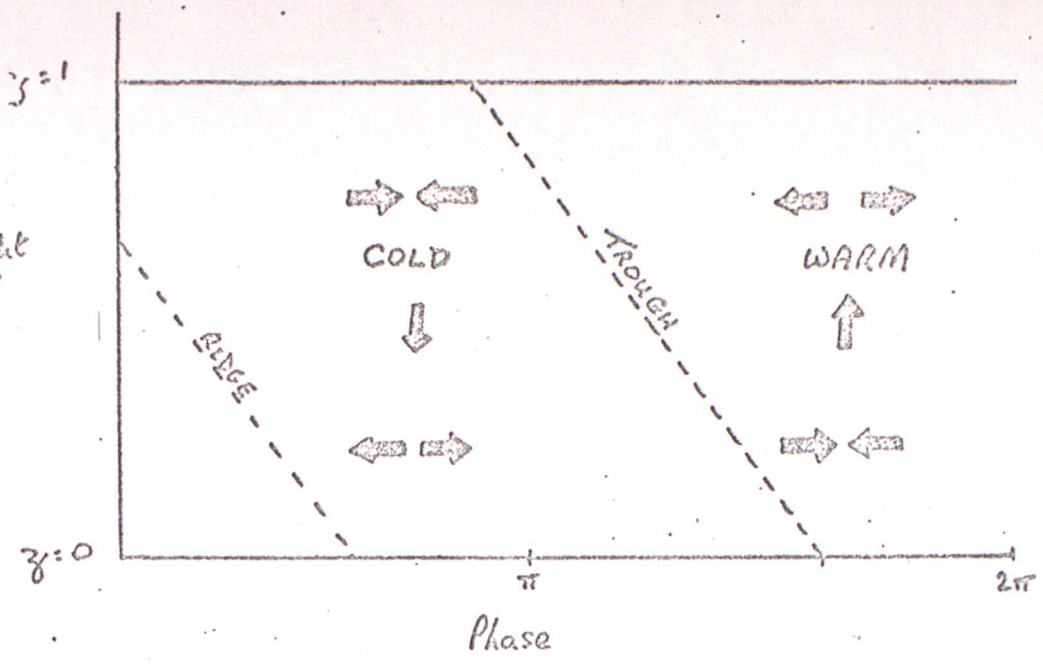
z = 1
Height
COLD
WARM
TROUGH
RIDGE
z = 0
π
2π
Phase

Fig 16

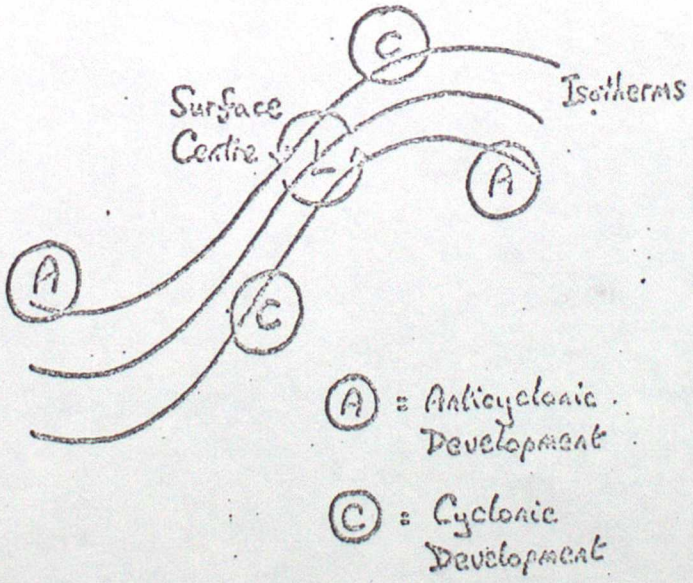
C
Surface
Centre
Isotherms
A
A
C
A = Anticyclonic Development
C = Cyclonic Development

Fig 17

950mb

750mb

LINEAR STAGE

DAYS 1-3

MATURE STAGE

DAYS 4-5

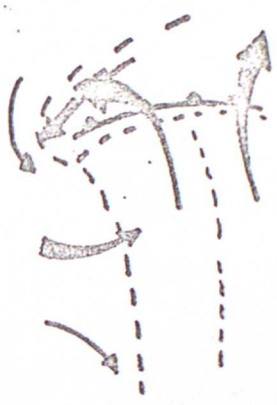

OCCLUDING STAGE

DAYS 6-

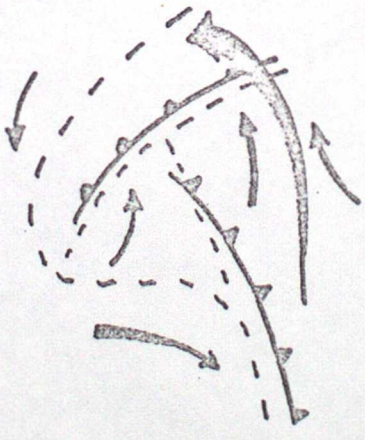

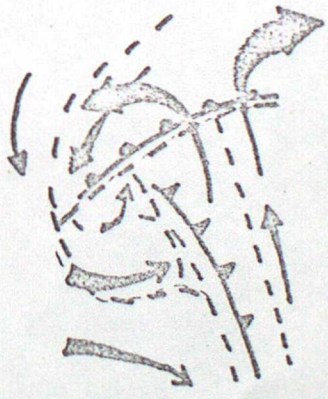

Fig 18